TU Delft

Delft University of Technology

Document Version
Final published version

Licence
CC BY

Citation (APA)
Tan, X., Xing, J., Mahjoubi, S., Guo, P., Wei, Z., Wang, Y., Ren, J., Ai, L., Meng, W., & Bao, Y. (2026). Explainable machine learning and life cycle assessment for sustainable design of fiber-reinforced asphalt concrete. *Journal of Cleaner Production*, *547*, Article 147759. https://doi.org/10.1016/j.jclepro.2026.147759

Important note
To cite this publication, please use the final published version (if applicable).
Please check the document version above.

Copyright
In case the licence states “Dutch Copyright Act (Article 25fa)”, this publication was made available Green Open Access via the TU Delft Institutional Repository pursuant to Dutch Copyright Act (Article 25fa, the Taverne amendment). This provision does not affect copyright ownership.
Unless copyright is transferred by contract or statute, it remains with the copyright holder.

Sharing and reuse
Other than for strictly personal use, it is not permitted to download, forward or distribute the text or part of it, without the consent of the author(s) and/or copyright holder(s), unless the work is under an open content license such as Creative Commons.

Takedown policy
Please contact us and provide details if you believe this document breaches copyrights.
We will remove access to the work immediately and investigate your claim.

This work is downloaded from Delft University of Technology.

Journal of Cleaner Production 547 (2026) 147759

Contents lists available at ScienceDirect

Journal of Cleaner Production

journal homepage: www.elsevier.com/locate/jclepro

Explainable machine learning and life cycle assessment for sustainable design of fiber-reinforced asphalt concrete

Xiao Tan [a,b], Jianglei Xing [a], Soroush Mahjoubi [c], Pengwei Guo [d,*], Ziyao Wei [e], Yuan Wang [a,b], Jie Ren [a,b], Li Ai [f,**], Weina Meng [g], Yi Bao [g]

[a] College of Water Conservancy and Hydropower Engineering, Hohai University, Nanjing, Jiangsu, 210024, China
[b] State Key Laboratory of Water Disaster Prevention, Nanjing, Jiangsu, 210024, China
[c] Department of Civil and Environmental Engineering, Massachusetts Institute of Technology, Cambridge, MA, 02139, United States
[d] Faculty of Civil Engineering and Geosciences, Delft University of Technology, Delft, 2628 CN, Netherlands
[e] Department of Civil and Environmental Engineering, University of Texas at Austin, Austin, TX, 78712, United States
[f] Department of Civil Engineering, The University of Texas Rio Grande Valley, Edinburg, TX, 78539, United States
[g] Department of Civil, Environmental and Ocean Engineering, Stevens Institute of Technology, Hoboken, NJ, 07030, United States

HIGHLIGHTS

- A dataset of 2490 laboratory samples was constructed for fiber-reinforced asphalt concrete.
- The dataset comprises 15 design parameters as inputs and 3 mechanical properties as outputs.
- 9 machine learning models were optimized using genetic algorithm for hyperparameter tuning.
- The SHAP algorithm and causal inference were used to interpret optimal predictions.
- A life cycle assessment was conducted to evaluate cost, carbon footprint, and energy efficiency.

GRAPHICAL ABSTRACT

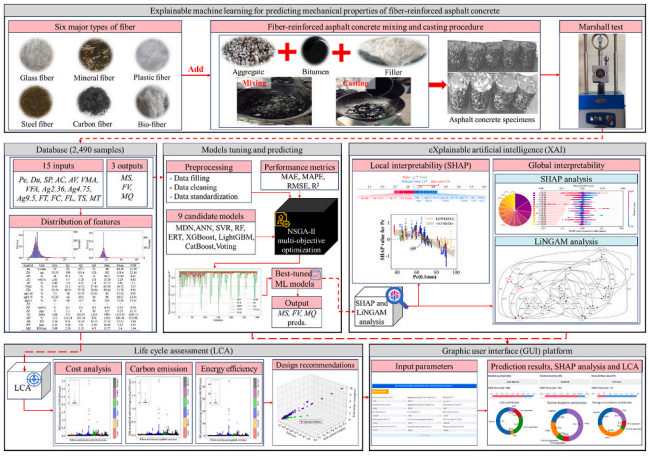

ARTICLE INFO

Keywords:
Fiber-reinforced asphalt concrete
Explainable artificial intelligence
Ensemble learning
SHAP analysis
Causal inference
Life cycle assessment

ABSTRACT

Conventional asphalt concrete has a limited lifespan due to cracking, deformation, and environmental degradation, driving the development of fiber-reinforced asphalt concrete (FRAC). However, key gaps remain in current data-driven FRAC studies due to small and homogeneous datasets, "black-box" machine learning models, and trade-offs between mechanical-sustainable performance, failing to provide a transparent understanding of features governing FRAC behaviors. This paper proposes a framework integrating explainable artificial intelligence and life cycle assessment (LCA) to advance mechanical and sustainable design of FRAC. A dataset of 2490

* Corresponding author.
** Corresponding author.
E-mail addresses: p.guo-1@tudelft.nl (P. Guo), li.ai@utrgv.edu (L. Ai).

https://doi.org/10.1016/j.jclepro.2026.147759
Received 18 October 2025; Received in revised form 18 January 2026; Accepted 7 February 2026
Available online 18 February 2026
0959-6526/© 2026 The Authors. Published by Elsevier Ltd. This is an open access article under the CC BY license (http://creativecommons.org/licenses/by/4.0/).

laboratory samples covers 15 input features and 3 mechanical outputs. Eight machine learning models, along with a voting ensemble strategy, were optimized using Genetic algorithm for hyperparameter tuning. The optimized voting ensemble achieved an average prediction performance of $R^2 = 0.87$, RMSE = 1.09, MAPE = 11.96%, and MAE = 0.60 across the three mechanical targets, indicating robust and reliable predictive capability. SHapley Additive exPlanations (SHAP) analysis and linear non-gaussian acyclic causal inference quantified global/local feature impacts and pairwise interactions. LCA evaluated economic and environmental impacts and derived strength-normalized sustainability metrics. Finally, an interactive graphic user interface platform was developed for predictions, SHAP interpretations, and LCA outcomes. This data-driven approach establishes a paradigm for intelligent FRAC design, harmonizing mechanical performance with sustainability.

Abbreviation List

Abbreviation	Full name
AC	Asphalt concrete
Ag2.36	2.36 mm aggregate passing rate
Ag4.75	4.75 mm aggregate passing rate
Ag9.5	9.5 mm aggregate passing rate
ANN	Artificial neural network
AV	Air voids
CART	Classification and regression tree
CatBoost	Categorical boosting
DAG	Directed acyclic graph
Du	Ductility
ERT	Extremely randomized trees
FC	Fiber content
FL	Fiber length
FRAC	Fiber-reinforced asphalt concrete
FT	Fiber type
FV	Marshall flow value
GBDT	Gradient boosting decision tree
GUI	Graphic user interface
KDE	Kernel density estimation
KNN	K-nearest neighbor
LCA	Life cycle assessment
LightGBM	Light gradient boosting machine
LiNGAM	Linear non-gaussian acyclic model
LOWESS	Locally weighted scatterplot smoothing
MAE	Mean absolute error
MAPE	Mean absolute percentage error
MDN	Mixture density network
ML	Machine learning
MQ	Marshall quotient
MS	Marshall stability
MT	Melting temperature
NSGA-II	Non-dominated sorting genetic algorithm II
PDF	Probability density function
Pe	Penetration
R^2	Coefficient of determination
RBF	Radial basis function
RF	Random forest
RMSE	Root mean square error
SHAP	SHapley Additive exPlanations
SP	Softening point
SVR	Support vector regression
TS	Tensile strength
VFA	Voids filled with asphalt
VMA	Voids in mineral aggregate
XAI	Explainable artificial intelligence
XGBoost	Extreme gradient boosting trees

1. Introduction

Asphalt concrete, with a global market value exceeding 3.4 billion U. S. dollars in 2024 (Asphalt Concrete Market Outlook, 2024), is widely used in road pavement (Wang et al., 2021), airport runways (AlKheder et al., 2022), parking lots (James and Thompson, 2021), and embankment dams (Ning et al., 2024) due to its crack resistance, waterproofing, quick repair, and cost-effectiveness (Bieliatynskyi et al., 2022; Yao et al., 2023; Rivera-Pérez et al., 2023). However, conventional asphalt concrete suffers from limited lifespan, brittleness in cold climates, and deformation under heat, making it prone to cracking from water damage, loading, aging, and temperature fluctuations (Ma et al., 2024a; Al-Atroush, 2022; Arabzadeh et al., 2016). To overcome these challenges, fiber-reinforced asphalt concrete (FRAC) has been developed, which has demonstrated improved toughness, crack resistance, and durability in numerous experimental studies (Ge et al., 2022; Wang et al., 2023; Jin et al., 2022a). Experimental studies have shown that FRAC with chopped fiber enhances Marshall stability by 17.4%, indirect tensile strength by 16.1%, and reduces rutting depth by 19% compared to conventional mixes (Takaikaew et al., 2018, 2021; Khan et al., 2023a, 2024; Mateos and Harvey, 2019). Incorporating waste fibers into asphalt concrete mitigates environmental burdens, since these non-degradable materials resist natural decomposition and can be effectively reused within asphalt mixtures (Takaikaew et al., 2018; Ma and Hesp, 2022; Ma et al., 2021, 2022, 2024b; Li et al., 2023).

Current experimental methods for evaluating FRAC are inefficient and costly, as any change in binder content, aggregate type, or gradation requires new, time-consuming laboratory tests (Dias et al., 2014; García et al., 2014; Liu and Wu, 2014; Pasandín and Pérez, 2015; Zaumanis et al., 2016; Wang et al., 2017). To determine the influence of fiber on mechanical performance, empirical formulas were developed to estimate mechanical behavior (Hejazi et al., 2008). Although the model demonstrates satisfactory fitting accuracy, its generalization capability is substantially constrained by two inherent limitations: simplified reinforcement mechanics based on an interface slip model and lack of sensitivity to mix design variability. Moreover, to assess the incorporation of fiber, researchers have examined its impact on fatigue resistance and rutting behavior. More advanced methods have adapted mechanistic-empirical frameworks like FlexPAVE™ to estimate the long-term fatigue and rutting performance of FRAC (Karanam and Underwood, 2024). Although these models offer accurate predictions, their reliance on fixed mix parameters severely restricts their adaptability (Khan et al., 2023b).

Recently, machine learning (ML) has been applied for material property prediction of FRAC, offering powerful predictive capabilities and a deeper understanding of the FRAC's complex behavior. ML models can analyze large, heterogeneous datasets to uncover the intricate, nonlinear relationships between mix parameters and mechanical properties (Upadhya et al., 2022). A variety of ML algorithms, including Artificial neural network (ANN) (Upadhya et al., 2024), Random forest (RF) (Upadhya et al., 2024), k-Nearest neighbor (KNN) (Phung et al., 2023a), Light gradient boosting machine (LightGBM) (Phung et al., 2023a), were used to predict the Marshall stability and indirect tensile strength of FRAC with remarkable accuracy. For example, RF predicted the Marshall stability of FRAC with R^2 of 0.83 (Upadhya et al., 2024), while KNN and LightGBM models achieved higher predictive accuracy with R^2 of 0.90 (Phung et al., 2023a). These methods outperform traditional empirical formulas, showing strong generalization across diverse mixture designs.

Despite these advancements, three key challenges hinder the broader adoption of MLs in FRAC design: (1) Small and homogeneous datasets remain a major limitation. Most existing studies rely on a few hundred samples with narrow material ranges, restricting generalization and increasing the risk of overfitting when predicting novel formulations. For instance, the dataset from Upadhya et al. only includes 164 data

points (Upadhya et al., 2022), which may increase the risk of model overfitting (Goodfellow et al., 2016). Besides, although some existing studies show high prediction accuracy, their results rely merely on single fiber type that cannot be transferred for other fiber categories (Upadhya et al., 2024; Phung et al., 2023a). (2) As shown in Fig. 1, many ML models lack interpretability as model complexity increases, known as the "black-box" effect. Particularly for ANN, while the model accuracy is higher than that of KNN and other regression models, the interpretability of ANN is limited due to the nonlinearity and complexity of the network structure (Lipton, 2018), making it difficult for engineers to identify how mix design parameters influence strength. Comprehensive experimental validation across diverse variables further adds cost and time burdens. (3) Although ML models were developed to predict the mechanical properties of FRAC (Upadhya et al., 2022; Upadhya et al., 2024; Phung et al., 2023a), existing studies focused mainly on mapping mixture design to material properties. Currently, sustainability considerations are rarely integrated, as life cycle assessment (LCA) is seldom incorporated into ML workflows, limiting holistic evaluation of FRAC in terms of both performance and environmental impact. Usually, incorporating supplementary materials in FRAC mixture designs shows a trade-off between mechanical properties and sustainability: Beneficial to sustainability but harmful to mechanical behaviors (Huang et al., 2007; Tan et al., 2022). It is unknown how FRAC mixtures should be engineered to optimize mechanical properties and sustainability for intended applications. These challenges are attributed to knowledge gaps in understanding of the effects of the mechanical and sustainable properties of FRAC on road and hydraulic infrastructure behaviors.

To address these challenges, this study introduces an innovative framework that integrates explainable artificial intelligence (XAI) and cradle-to-gate LCA to simultaneously advance the mechanical performance and sustainability of FRAC. The research objectives are threefold: (1) Develop a data-driven machine learning framework based on a large and comprehensive dataset to evaluate strength-normalized sustainability metrics of FRAC systems with varying ingredients and mix proportions. In this work, nine machine learning models are adopted, such as Mixture density network, Support vector regression, and Extreme gradient boosting trees, along with a voting ensemble strategy. The hyperparameters are optimized via Non-dominated Sorting Genetic Algorithm II (NSGA-II) for multi-objective tuning. (2) Apply an XAI approach that leverages the SHapley Additive exPlanations (SHAP) algorithm and Linear Non-Gaussian Acyclic Model (LiNGAM) causal inference to enhance dataset interpretation and uncover feature interactions. (3) Evaluate the life-cycle performance of FRAC through a cradle-to-gate analysis considering cost, carbon emissions, and energy consumption throughout the service life. Based on LCA, the optimal asphalt concrete fiber additives and FRAC mixture designs were identified based on economic, environmental, and performance perspectives.

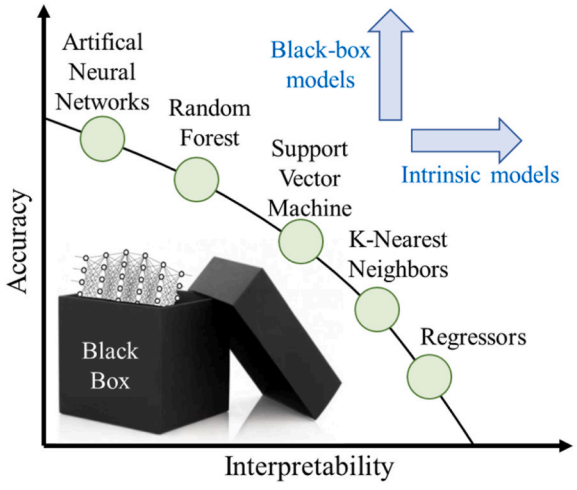

Fig. 1. Trade-off between model accuracy and interpretability in machine learning models.

To achieve the above objectives, a large dataset of 2490 samples containing mechanical (Marshall stability, flow value, Marshall quotient), economic (unit price), and environmental metrics (carbon footprint and energy consumption) was used to train and evaluate nine ML models. The SHAP and causal inference algorithms were utilized to interpret predictions and clarify the influence of input features including their pairwise interactions. Finally, a graphic user interface (GUI) platform was developed to generate recommendations on the ranges of design variables for frontier practitioners by evaluating the impacts of design variables on the mechanical performance and sustainability of FRAC.

The key novelties of this research can be summarized as follows: (1) Development of an XAI framework, integrating advanced data preprocessing methods (missing data interpretation, data standardization and splitting, and feature extraction), machine learning methods (ensemble learning based on voting model, hyperparameter tuning based on multi-objective optimization), and model interpretation methods (SHAP analysis and causal inference). Four different types of base models are selected to form a voting ensemble model through a weighted average. NSGA-II is used to simultaneously maximize the R^2 values of three output variables. (2) Establishment of a large and comprehensive dataset with six sub-datasets based on fiber categories for the first time, including glass fiber, mineral fiber, plastic fiber, steel fiber, carbon fiber, and bio-fiber. (3) A user-friendly GUI platform embedding a XAI-driven design recommendation tool is developed for engineers to remove professional barriers and to implement interactive prediction results.

The remainder of the paper is organized as follows: Section 2 presents the methodology. Section 3 presents and discusses the results. Section 4 develops the graphic user interface platform. Section 5 summarizes the limitations and recommends future research opportunities. Section 6 provides a summary of the conclusions.

2. Methodology

2.1. Research framework

Fig. 2 shows the flowchart of the developed framework in this study, including four main steps: **(1) Dataset preprocessing:** The dataset derived from FRAC literature, includes mixture design parameters as inputs and Marshall stability (*MS*), flow value (*FV*), and quotient (*MQ*) as outputs. Missing values were imputed and data standardized to ensure consistency and quality. **(2) Model tuning and prediction:** Nine ML models, including eight single models and a voting model combining four of them, underwent training and evaluation. The NSGA-II algorithm was utilized for multi-objective optimization to boost their effectiveness. Ultimately, the accuracy of these nine models in predicting the performance of FRAC was compared. **(3) Explainable artificial intelligence:** SHAP analysis was employed to provide global insights and quantify feature importance, while causal inference based on LiNGAM was used to reveal interactions among design variables affecting FRAC performances. **(4) Life cycle assessment and design recommendations:** At the mixture design stage, cost, carbon footprint, and energy use of FRAC were evaluated to optimize sustainability, with *MQ*-normalized metrics guiding resource-efficient design recommendations.

2.2. Dataset preparation

2.2.1. Dataset collection and description

A comprehensive database comprising 2490 FRAC samples was compiled from relevant published studies for predicting *MQ*, *MS*, and *FV*. These datasets were derived from 141 articles published between

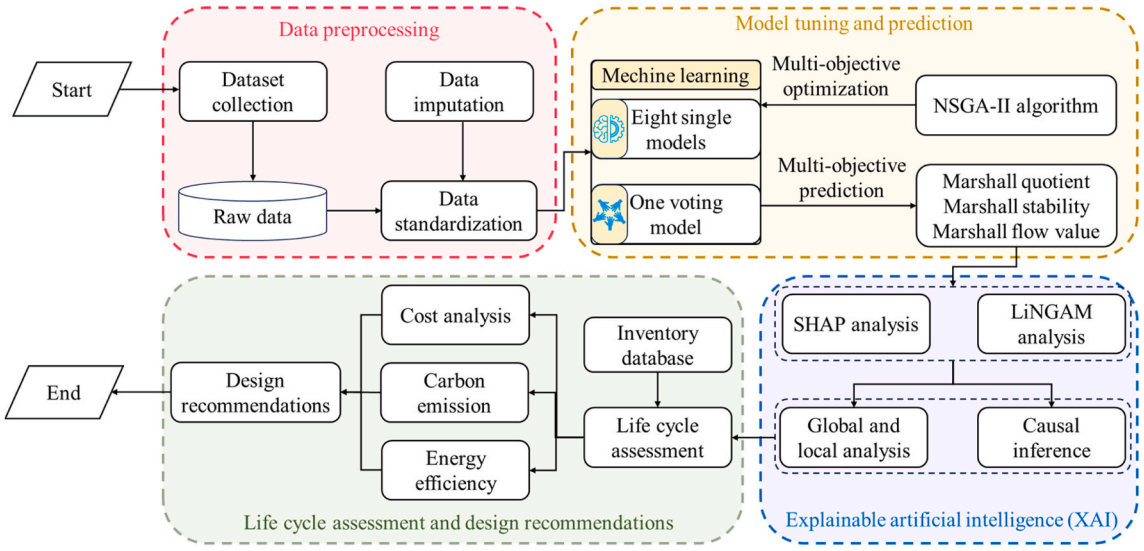

Fig. 2. Flowchart of the proposed framework integrating multi-model prediction, explainable artificial intelligence, and life cycle assessment.

2002 and 2025, which can be found in Supplementary materials. In these studies, the *MS* and *FV* of FRAC are directly obtained through specimen testing, while *MQ* is calculated as the ratio of *MS* to *FV* (*MQ*=*MS*/*FV*). Considering the inherent properties of asphalt, aggregate gradation, and fiber characteristics, this dataset comprises fifteen input features and three output features to investigate their effects on FRAC (Phung et al., 2023b). The fifteen input features are penetration (*Pe*), ductility (*Du*), softening point (*SP*), asphalt content (*AC*), air voids (*AV*), voids in mineral aggregate (*VMA*), voids filled with asphalt (*VFA*), the passing rates of 2.36 mm, 4.75 mm, and 9.5 mm aggregates (*Ag2.36*, *Ag4.75*, and *Ag9.5*), fiber type (*FT*), fiber content (*FC*), fiber length (*FL*), tensile strength (*TS*), and melting temperature (*MT*). In addition, there is a wide variety of fiber types, which can be classified into six major categories, namely glass fiber, mineral fiber, plastic fiber, steel fiber, carbon fiber and bio-fiber. Among them, mineral fiber, plastic fiber and bio-fiber are further divided into many subtypes. The number of various fiber samples is shown in Table A1.

2.2.2. Data analysis

Fig. A1 illustrates the missing data ratios of different features. The missing values are handled in two categories. For asphalt and aggregate features, missing entries are imputed using the overall average value of the dataset. For fiber-related features, the data are divided into six sub-datasets based on fiber types (see Table A1), and missing values within each sub-dataset are replaced by the corresponding subgroup mean. After imputation, Table 1 summarizes the statistical distribution of all variables, including minimum, maximum, quartiles, mean, and standard deviation.

Fig. A2 displays the probability density distributions of the fifteen input features and three output variables. Each subplot uses a dual-axis design to show the distribution of features (e.g., *Pe*, *Du*, *SP*). The left primary axis displays the probability density function, and the right secondary axis shows the frequency distribution. A Pearson correlation analysis was conducted to assess multicollinearity, as presented in Fig. 3 (Benesty et al., 2009). Results show that, apart from a few aggregate passing rates with strong correlations, most input features exhibit weak relationships ($|R| < 0.7$) (Guo et al., 2024). This suggests limited linear dependence and low redundancy, supporting the suitability of the chosen features for model training. Since excessive input correlation can reduce both predictive accuracy and interpretability, all mixture design variables were retained as model inputs (Zhou et al., 2024).

2.2.3. Data preprocessing

To prepare the dataset for machine learning analysis, the feature Fiber Type (*FT*) was encoded as integer labels representing six distinct fiber categories: 1 – Glass fiber; 2 – Mineral fiber; 3 – Plastic fiber; 4 –

Table 1
Distribution of fifteen input features and three output features.

Symbol	Unit	Min	Q1	Q2	Q3	Max	Mean	STD
Pe	0.1 mm	37	63	67.7	74	98	68.48	13.49
Du	cm	50.33	100	111.4	120	182	111.4	22.16
SP	°C	41	47.1	50	52	88.5	51.99	8.85
AC	% by mass	2.85	4.7	5.19	5.8	10.39	5.29	0.91
AV	%	0.03	3.6	4.47	5.4	21.73	4.85	2.5
VMA	%	8.33	15.2	16.72	17.44	62.96	16.72	3.17
VFA	%	13.24	68.11	71.78	76.84	99.64	71.78	9.91
Ag2.36	%	7.5	30	35.53	42.93	85	35.53	9.42
Ag4.75	%	17.32	42	49.3	56	95	48.17	12.94
Ag9.5	%	35	68	74.7	80	100	72.38	13.02
FT	/	/	/	/	/	/	/	/
FC	%	0	0.1	0.3	0.5	6.94	0.45	0.76
FL	mm	0	1.1	6	10	125	8.23	11.37
TS	MPa	0.08	375	563.91	2320	4900	1255.07	1300.72
MT	°C	155	214.28	247.54	850	3500	666.38	872.98
MS	kN	0.34	9.31	11.24	14.55	35.42	12.25	4.49
FV	mm	1.42	3.08	3.6	4.36	36.83	4.32	2.97
MQ	kN/mm	0.08	2.26	3.19	4.3	10.27	3.4	1.64

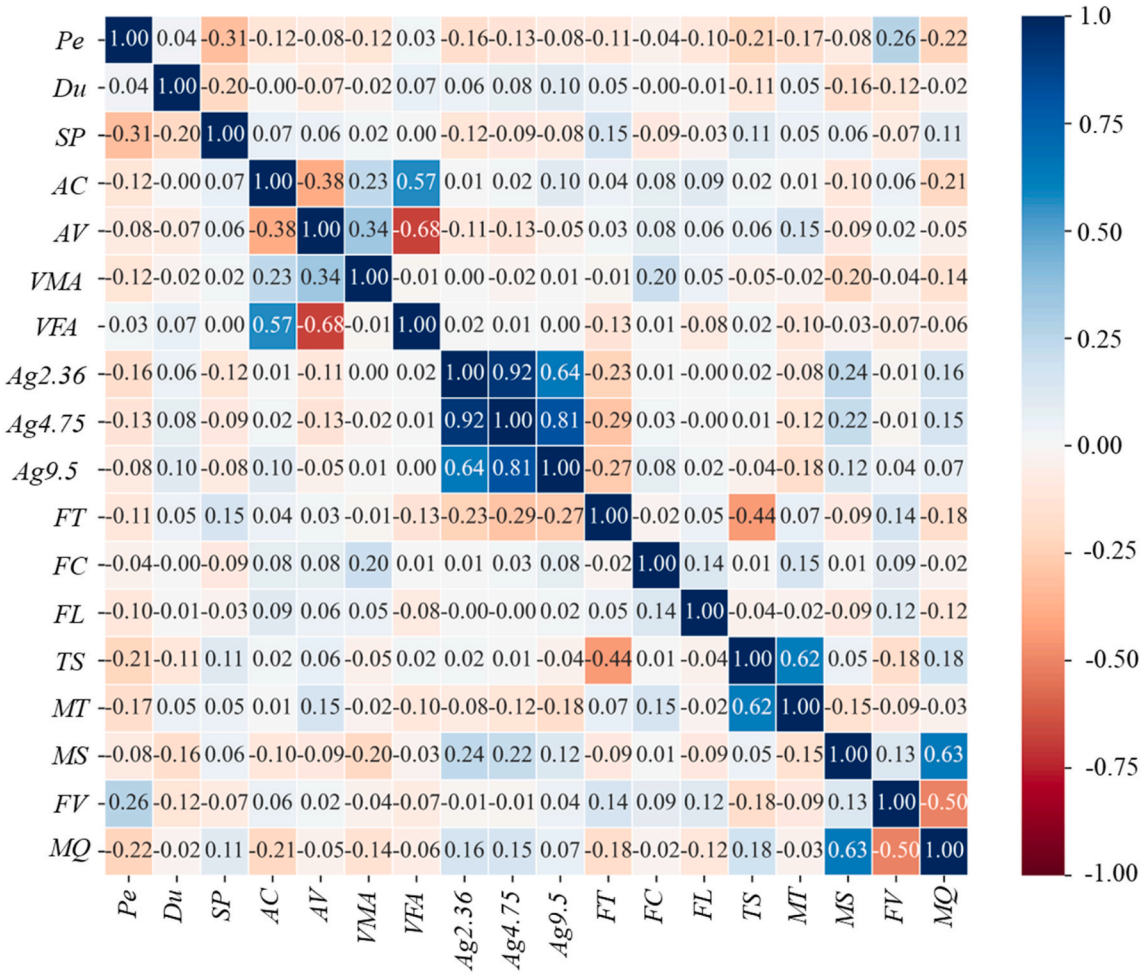

Fig. 3. Heatmap of Pearson correlation coefficient of dataset.

Steel fiber; 5 – Carbon fiber; and 6 – Bio-fiber. This numeric encoding allowed the categorical feature to be effectively processed by the learning algorithms.

Data standardization is a crucial step in machine learning, as it ensures that variables with different scales are transformed into a standard range. This standardization can help in achieving faster convergence by preventing the algorithm from being dominated by variables on a larger scale (Singh and Singh, 2020). There are several common techniques for data normalization, such as Decimal scaling, Min-max scaling, Max-abs scaling and Z-score scaling (Jain et al., 2005). In this study, two scalers, the Max-abs scaling (z_1) and Z-scaling (z_2), were used to standardize the X input values for the MDN and the other eight models, respectively. The formulas for two scalers are shown as follows:

$$z_1 = \frac{x - m}{\sigma} \tag{1}$$

$$z_2 = \frac{x - m}{max(x)} \tag{2}$$

where x is an input variable; m and σ are the average and standard deviation of x.

Since the MDN model's predictions consist of three mixture components (weight π, mean μ, and standard deviation σ), and σ can become too small, causing $\log(\sigma)$ to approach negative infinity and leading to gradient explosion, a Z-scaler was applied to scale the MDN's y values to a standard deviation of 1. This helped to avoid gradient explosions.

Then, the standardized dataset was shuffled to avoid order bias and ensure a representative training set (Zhou et al., 2024). The shuffled dataset was split into 80% for training purposes and 20% for testing (Ejaz et al., 2024). The dataset was evaluated using a fixed random seed (random state = 42) to ensure reproducibility.

2.3. Machine learning algorithms

Eight machine learning models are adopted in this research: Support Vector Regression (SVR) (Cortes and Vapnik, 1995), Random Forest (RF) (Zhou et al., 2024), Extremely Randomized Trees (ERT) (Geurts et al., 2006), Extreme Gradient Boosting Trees (XGBoost) (Chen and Guestrin, 2016), Categorical Boosting (CatBoost) (Prokhorenkova et al., 2018), Light Gradient Boosting Machine (LightGBM) (Ke et al., 2017), Artificial Neural Network (ANN) (Kaveh, 2024), and Mixture Density Network (MDN) (Bishop, 1994). These methods can be categorized into single models (SVR, ANN, MDN) and ensemble models (RF, ERT, XGBoost, CatBoost, LightGBM), as summarized in Table 2.

2.4. Ensemble learning based on voting model

Voting is an ensemble learning technique that combines multiple machine learning models to enhance predictive performance (Calvert, 1985). In this method, base models are trained on the dataset to generate individual predictions. The voting model makes predictions based on the weighted average of outputs from heterogeneous base models. This process allows voting model to leverage the unique strengths of each base model, reducing variance and improving generalization (Bartlett et al., 1998).

In this study, in order to improve the generalization performance and

Table 2
Summary of machine learning models.

No.	Model	Category	Notes
1	ANN	Classical	Kernel-based regression
2	SVR	Classical	Nonlinear regression
3	MDN	Classical	Probabilistic neural network
4	RF	Ensemble – Bagging	Bagging of decision trees
5	ERT	Ensemble – Bagging	Variant of RF with more randomization
6	XGBoost	Ensemble – Boosting	Gradient boosting with regularization
7	CatBoost	Ensemble – Boosting	Gradient boosting optimized for categorical features
8	LightGBM	Ensemble – Boosting	Efficient histogram-based gradient boosting

robustness through model heterogeneity (Dietterich, 2000), four base models of different types (ERT, LightGBM, ANN, and SVR) were selected from the above eight models to form a voting model, as illustrated in Fig. 4. Specifically, each of the four base models generates a prediction result, which are then combined using a weighted averaging scheme. In this process, each prediction is multiplied by a corresponding weight, and the resulting values are summed to produce the final prediction. The weights are determined based on the performance of the individual base models. By consolidating the predictions from the four base models, voting model is able to capture complex patterns and uncertainties, thereby generating a comprehensive final prediction. This integration of predictions from high-performing and heterogeneous base models enhances the generalization capability of the voting model in multi-objective regression tasks.

2.5. Evaluation metrics

Model performance was assessed using four metrics: Mean Absolute Error (MAE), Root Mean Square Error (RMSE), Mean Absolute Percentage Error (MAPE), and the coefficient of determination (R^2). The corresponding formulas are provided in Eq. (3) to Eq. (6). MAE reflects the average magnitude of prediction errors in the same unit as the target variable, providing an intuitive measure of typical deviation. RMSE is the square root of the average squared differences between predicted and actual values, placing greater emphasis on larger errors and thus offering sensitivity to outliers. MAPE represents prediction error as a percentage of the actual values, enabling scale-independent evaluation and relative interpretation of accuracy. R^2 quantifies the proportion of variance in the target variable explained by the model, where values closer to one indicate stronger explanatory power. In general, lower MAE, RMSE, and MAPE denote higher accuracy, while higher R^2 suggests a better model fit.

$$RMSE = \sqrt{\frac{1}{n}\sum_{i=1}^{n}\left(y_{i,pre} - y_{i,test}\right)^2} \tag{3}$$

$$MAPE = \frac{1}{n}\sum_{i=1}^{n}\left|\frac{y_{i,pre} - y_{i,test}}{y_{i,test}}\right| \times 100\% \tag{4}$$

$$MAE = \frac{1}{n}\sum_{i=1}^{n}\left|y_{i,pre} - y_{i,test}\right| \tag{5}$$

$$R^2 = 1 - \frac{\sum_{i=1}^{n}\left(y_{i,test} - y_{i,pre}\right)^2}{\sum_{i=1}^{n}\left(y_{i,test} - \bar{y}\right)^2} \tag{6}$$

where $y_{i,test}$ and $y_{i,pre}$ are the tested and predicted *MQ*, respectively; $\bar{y}$ is the average *MQ* of FRAC in the dataset; n is the number of samples in the dataset.

2.6. Hyperparameter tuning based on multi-objective optimization

Hyperparameter tuning is critical for optimizing machine learning models. Common approaches include Grid Search (Sun et al., 2021) and Random Search (Bergstra and Bengio, 2012), Bayesian Optimization (Wu et al., 2019), etc. Grid Search and Random Search are unsuitable for the multi-objective optimization in this study, meanwhile Bayesian Optimization is computationally impractical for the large dataset (2490 samples). Therefore, the NSGA-II algorithm, a Genetic Algorithms-based method, is employed. NSGA-II efficiently handles multiple objectives by using a non-dominated sorting and crowding distance to maintain solution diversity (Deb et al., 2000). It explores the hyperparameter space by evolving generations of solutions. Each "individual" in a population represents a potential hyperparameter combination (e.g., the n_estimators and learning_rate of LightGBM, or the hidden_layer_sizes of ANN in

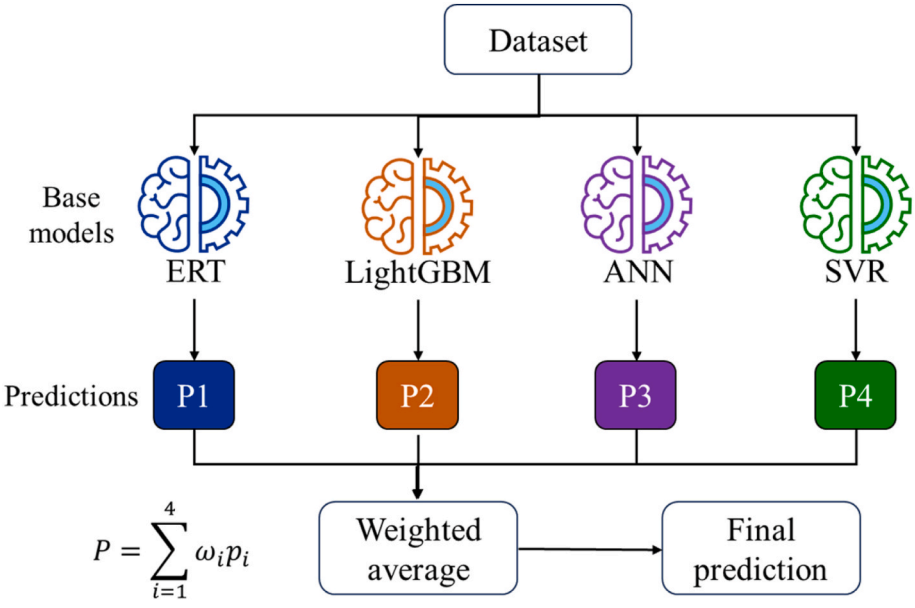

Fig. 4. Schematic diagram of voting ensemble learning.

this study). In this work, the goal is to maximize the R^2 values of three output variables (*MQ, MS, FV*) simultaneously. The objective functions are defined as:

$$\begin{cases} f_1(X) = R^2_{MQ}(X) \\ f_2(X) = R^2_{MS}(X) \\ f_3(X) = R^2_{FV}(X) \end{cases} \tag{7}$$

where X denotes a hyperparameter combination, and $R^2_{MQ}(X)$, $R^2_{MS}(X)$, $R^2_{FV}(X)$ are the R^2 scores of *MQ*, *MS*, and *FV* predicted by the model with hyperparameters X, respectively.

Through selection, crossover, and mutation operations, the algorithm evolves these individuals to find optimal hyperparameter sets. The selection is guided by non-dominated sorting, which classifies solutions into different fronts based on "dominance relations". For two hyperparameter combinations X_a and X_b, X_a is said to dominate X_b (denoted as $X_a < X_b$) if:

$$\begin{cases} f_i(X_a) \geq f_i(X_b) & \forall i \in \{1,2,3\} \\ f_j(X_a) > f_j(X_b) & \forall j \in \{1,2,3\} \end{cases} \tag{8}$$

In the context of this study, this means X_a achieves better or equal R_2 values for all three objectives (*MQ, MS, FV*) compared to X_b, and strictly better for at least one objective.

To maintain diversity in the Pareto-optimal set, NSGA-II calculates the crowding distance for each solution, which measures the density of surrounding solutions. For a solution X_i in the k-th front, its crowding distance d_i is:

$$d_i = \sum_{m=1}^{3} \frac{f_m(X_{i+1}) - f_m(X_{i-1})}{f_m^{max} - f_m^{min}} \tag{9}$$

where $f_m(X_{i-1})$ and $f_m(X_{i+1})$ are the m-th objective values of the neighbors of X_i (sorted by the m-th objective), and f_m^{max}, f_m^{min} are the maximum and minimum values of the m-th objective in the k-th front. This ensures the final solutions cover diverse trade-offs.

This method provides a set of Pareto-optimal solutions, giving insights into the trade-offs between different objectives (Antkiewicz and Myszkowski, 2024). NSGA-II is well-suited for this study's multi-objective regression tasks, offering effective hyperparameter optimization for the models used. The flowchart of hyperparameter tuning is shown in Fig. 5.

2.7. SHAP-based model explanation

Machine learning models show strong predictive performance in material engineering but are often hindered by limited interpretability, as they function like "black boxes". Post-hoc methods such as SHAP (Lundberg and Lee, 2017) address this by assigning importance scores to features, enabling both global and local interpretability of model outcomes. Fig. 6 depicts the workflow for the explainable prediction process using SHAP algorithm. Fig. 6(a) shows the "black-box" model prediction, where inputs like *FC*, *FL*, *Ag9.5*, *Pe*, etc., generate an *MQ* prediction of 4.32. Fig. 6(b) introduces SHAP interpretation, converting the prediction into an interpretable form by calculating SHAP values, which quantify each feature's contribution. Fig. 6(c) details these SHAP values, showing how they adjust the average model output (3.41) through positive or negative contributions (e.g., $X_1 = -0.05$, $X_2 = +0.05$) to reach the final prediction. Fig. 6(d) displays a SHAP waterfall plot, visually representing the calculation process. The "average prediction" serves as a baseline, with red (positive) and blue (negative) bars showing how each feature shifts the output toward the final value, providing transparency into the model's decision process.

2.8. Causal inference

Causal inference is an important method for uncovering the causal relationships between 15 input variables and 3 objectives. A linear non-gaussian acyclic model (LiNGAM) was employed to infer the causal directed acyclic graph (DAG) (Shimizu et al., 2006), thereby elucidating the latent causal architecture linking the investigated factors to *MQ, MS* and *FV*. As illustrated in Fig. 7, this DAG schematic diagram discloses the causal interactions between six black input variables and three red output variables. Nodes represent observed quantities, and directed edges together with their weights quantify both the direction and strength of causal influence; positive weights indicate promotion, whereas negative weights indicate suppression. The causal relationships identified by the model converge with the SHAP-derived attributions, thereby furnishing mutually reinforcing evidence that enhances the robustness and reliability of the inferred causal structure.

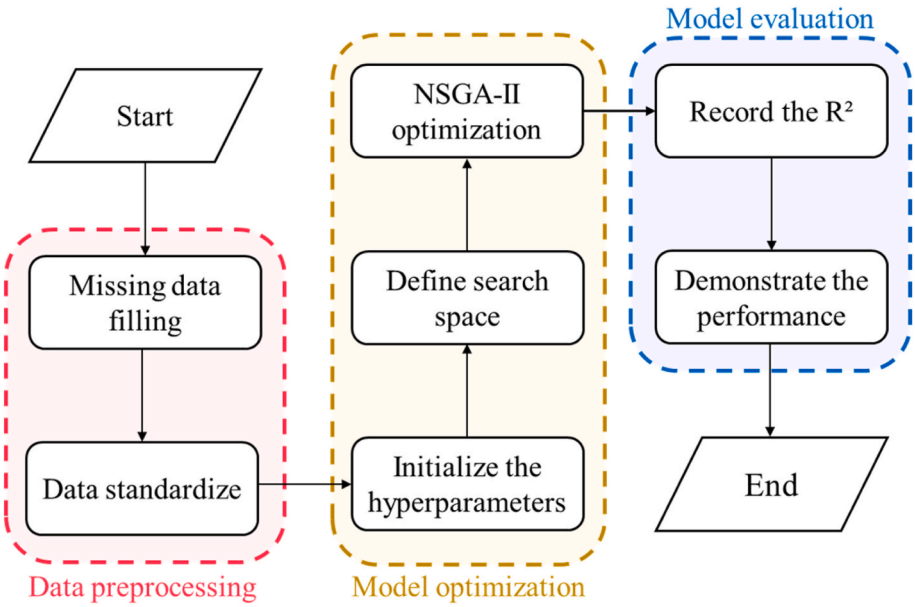

Fig. 5. The flowchart of hyperparameter tuning process based on multi-objective optimization.

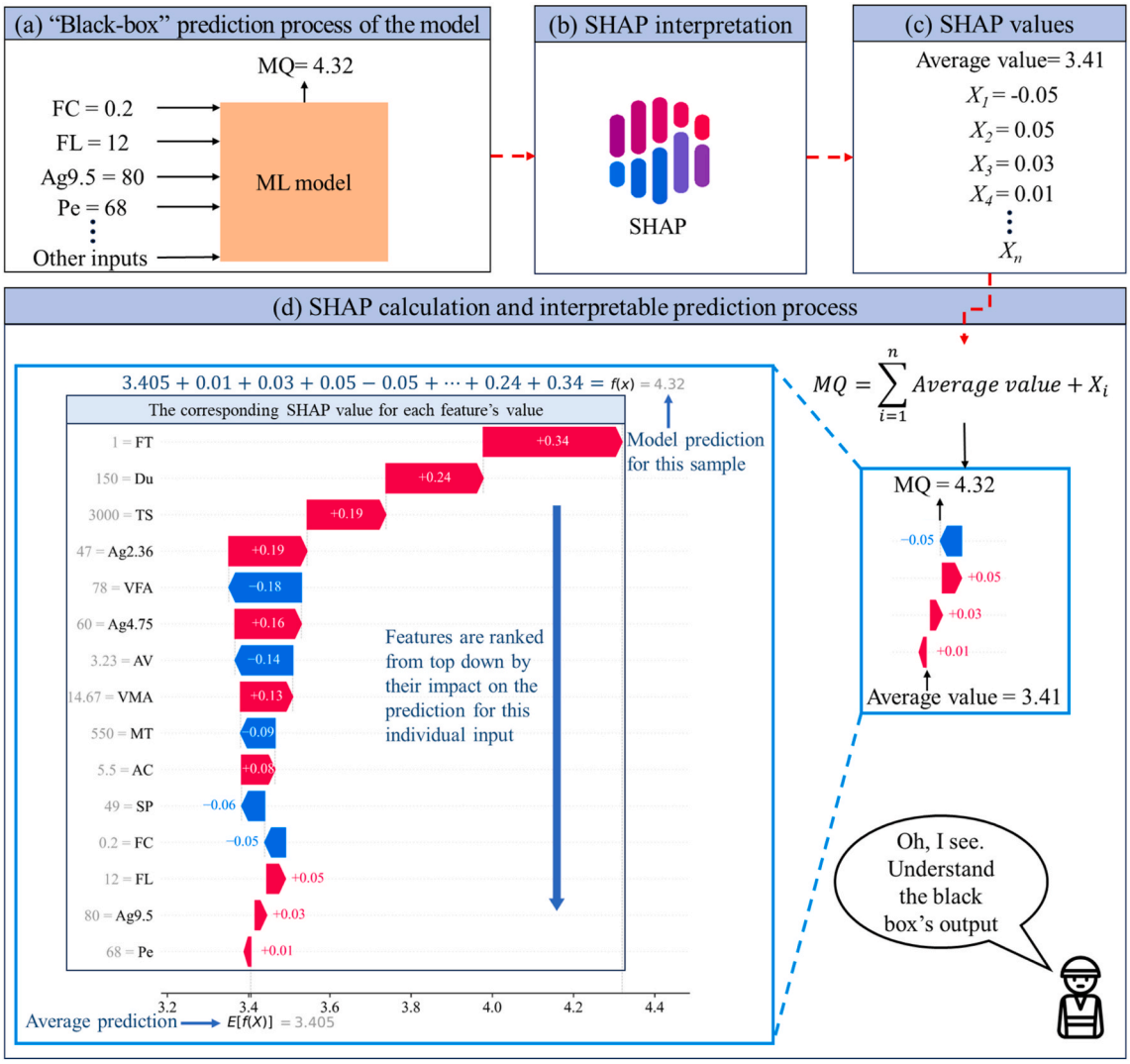

Fig. 6. Flowchart of SHAP algorithm explanation for the machine learning model predictions.

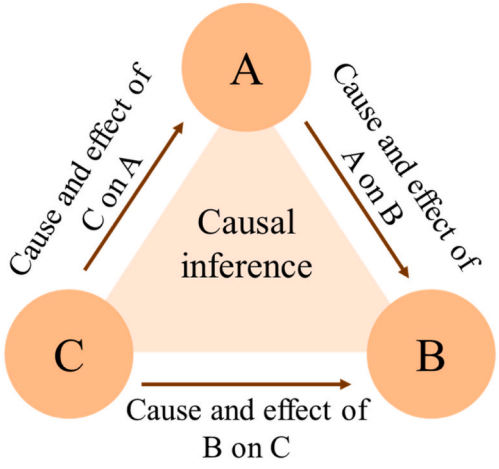

Fig. 7. The DAG diagram generated by the LiNGAM algorithm.

2.9. Life cycle assessment

This study adopts a cradle-to-gate boundary, focusing exclusively on the production phase of FRAC and excluding the construction, use, and end-of-life stages. This scope enables a targeted assessment of the material's early economic and environmental impacts. The analysis emphasizes key sustainability indicators—cost, carbon emissions, and energy consumption—while also examining the relationship between environmental impact and mechanical performance by comparing *MQ* per unit of material.

The total cost, carbon emissions, and energy consumption for producing 1 kg FRAC under standard curing conditions are calculated using Eq. (10) to Eq. (12), respectively. To assess resource efficiency, strength-normalized indicators are calculated by combining the *MQ* with the corresponding environmental and economic impacts. These indicators offer a robust basis for comparing the cost and environmental performance of FRAC formulations. The developed machine learning model is initially used to predict the *MQ* of FRAC, and subsequently to support strength-normalized LCA.

$$M = \sum_{i=1}^{n} m_i r_i \tag{10}$$

$$C = \sum_{i=1}^{n} c_i r_i \tag{11}$$

$$E = \sum_{i=1}^{n} e_i r_i \tag{12}$$

where M, C, E denote the cost, CO_2 emission, equivalent energy consumption of producing 1 kg FRAC, respectively; m_i, c_i, e_i are the unit cost, CO_2 emission, energy consumption used to produce the ith ingredient ($i = 1, 2, \ldots, n$); and r_i is the mass of the ith ingredient.

Optimal material usage can be identified by evaluating three performance indicators: strength-normalized cost, carbon footprint, and energy consumption. For each mixture, the total cost, carbon footprint, and energy consumption are calculated by summing the contributions of individual materials based on their unit impacts. These totals are then normalized by the *MQ* to produce three strength-normalized indicators. Boxplots for each indicator are used to determine their lower quartile (Q1 = 25%) thresholds. Mixtures that fall below the Q1 thresholds for all three indicators are considered to have balanced, low environmental and economic impacts. By identifying the minimum and maximum usage values for each material across these optimal mixtures, the approach defines intersection ranges that represent the most sustainable and cost-effective usage levels for practical applications.

3. Results and discussion

3.1. Hyperparameter tuning results

To identify the optimal hyperparameter combinations, each model underwent 300 iterations of NSGA-II optimization. The algorithm was configured with a population size of 100, employing simulated binary crossover with a crossover probability of 0.9 and a distribution index of 20, as well as polynomial mutation with a mutation probability of 0.15 and a distribution index of 15. These parameter settings follow the widely recommended defaults in NSGA-II literature (Deb et al., 2002).

In addition, the maximum number of generations was set to 300 as the termination criterion. Tests showed that the optimization curves of all models converged well before 300 generations, with no meaningful improvement in R^2 beyond approximately 250 generations. Therefore, 300 generations provided sufficient evolutionary depth without unnecessary computation.

Fig. 8 records the average R^2 scores for predicting the three objectives on the testing set, based on the number of iterations in the NSGA-II process. As observed, after 300 iterations, while the MDN model still showed some fluctuation, the R^2 values of the other eight models stabilized above 0.8, indicating strong performance.

Fig. 9 illustrates the three-dimensional Pareto front for the nine models in terms of *MQ*, *MS*, and *FV* optimization. The Pareto front is composed of the scatter points shown in the figure, where each point represents a non-dominated solution. Improving one objective often requires trade-offs with others, and each point reflects an optimal balance among the three objectives.

The red pentagram denotes the best point on the Pareto front, representing the most desirable solution with the highest overall performance across the three objectives. For example, the LightGBM model excels in maximizing *FV* (R^2), while the ERT model performs better in enhancing *MQ* (R^2) and *MS* (R^2). Notably, the voting model integrates predictions from ERT, LightGBM, SVR, and ANN, all with previously optimized hyperparameters, resulting in a narrow Pareto front range in the figure. This highlights its consistently high performance. By employing the NSGA-II algorithm, which uses non-dominated sorting and crowding distance to maintain diversity in the solution space, we can efficiently locate these Pareto optimal solutions. This ensures a well-distributed set of optimal solutions along the Pareto front, allowing researchers and practitioners to choose model configurations that best meet their specific needs regarding *MQ*, *MS*, and *FV*. Finally, by selecting the hyperparameter values that yield the highest average R^2, the optimal configurations are finalized and presented in Table B1.

3.2. Prediction performance

Fig. 10 illustrates the performance of nine machine learning models in predicting *MQ* on both training and testing datasets. The prediction performance for *MS* and *FV* is presented in Fig. B1 and Fig. B2, respectively. The blue and red dots in the figure show the relationship between predicted and actual values for the training and testing sets, respectively. Points on the black diagonal line indicate perfect predictions where predicted and actual values are equal. The closer the points are to this line, the smaller the error produced by the ML model, reflecting better predictive performance. This visualization evaluates model accuracy, with results satisfying the accepted criterion for ML models that MAE remains smaller than RMSE (Khan et al., 2022).

In general, except for the MDN model, the other eight models demonstrate exceptional predictive accuracy for *MQ* of FRAC. Their R^2 values exceed 0.93 on the training set and 0.83 on the testing set.

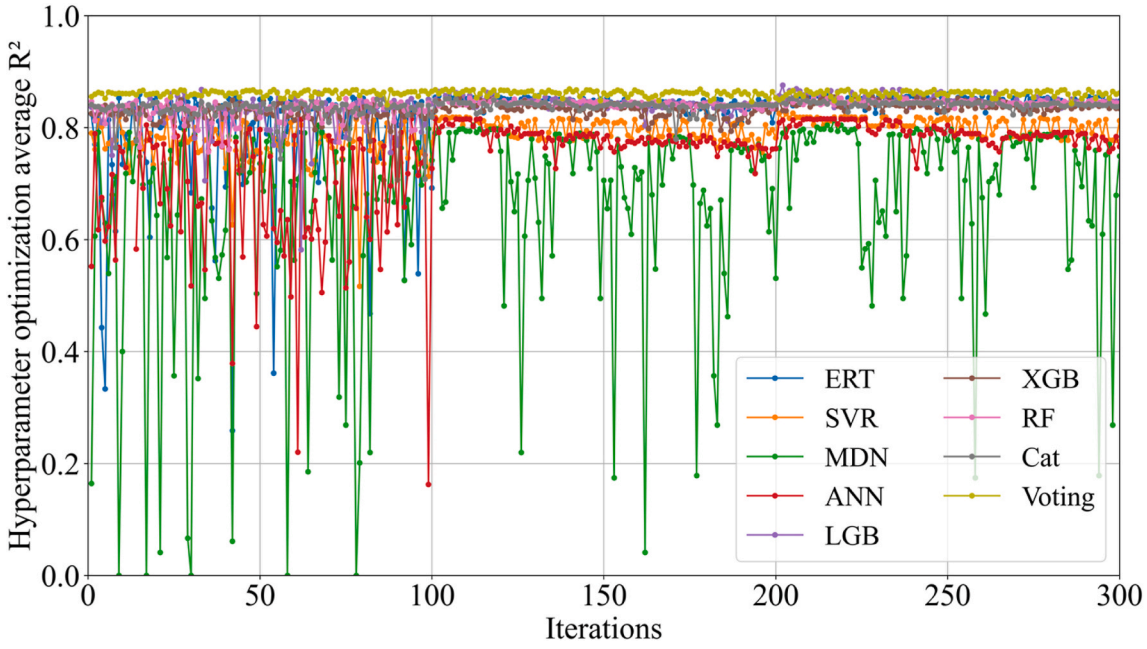

Fig. 8. R^2 scores of the nine models in iterations process using the NSGA-II algorithm.

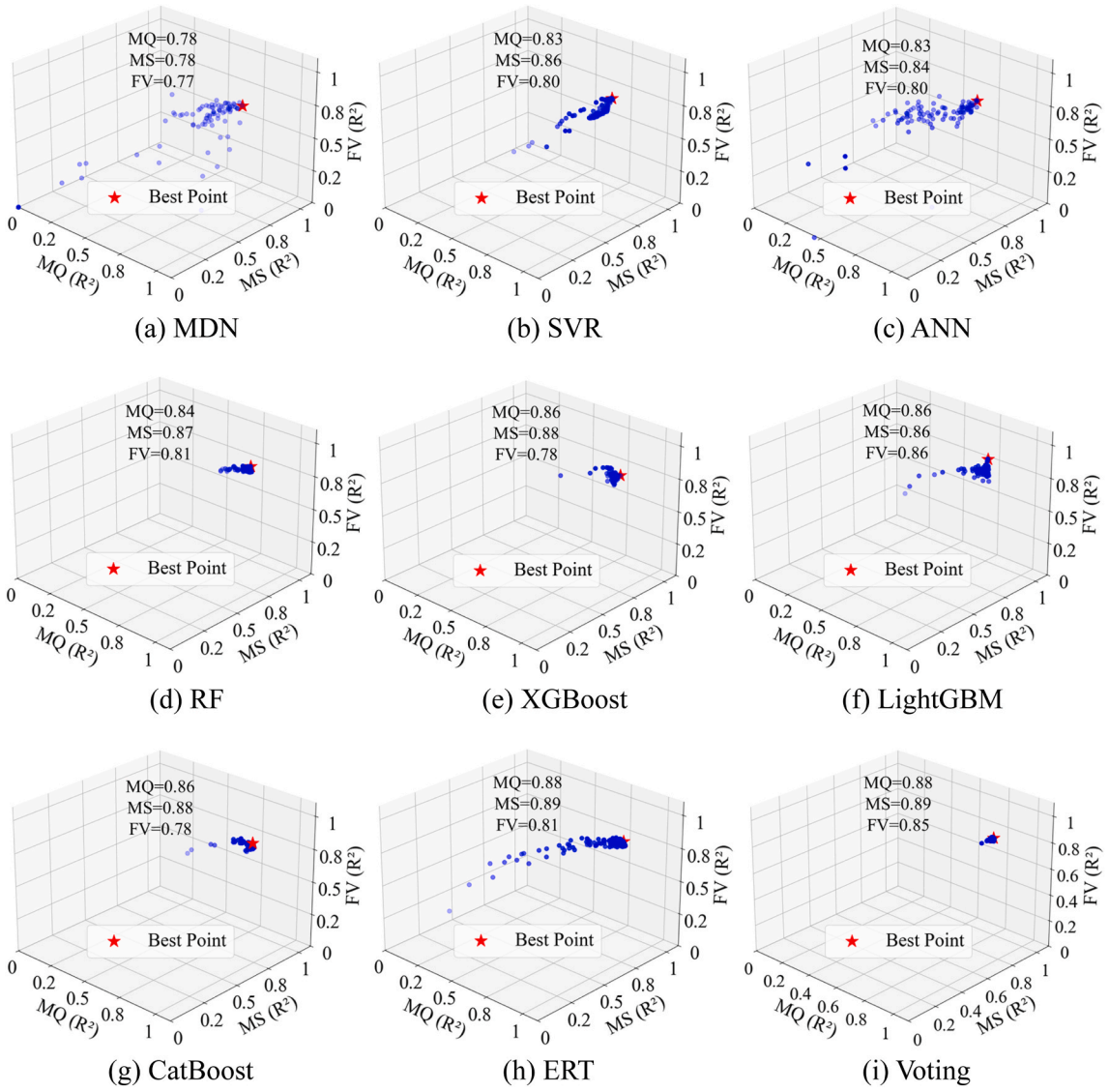

Fig. 9. Three-dimensional Pareto front diagram of *MQ*, *MS* and *FV* of the nine models: (a) MDN; (b) SVR; (c) ANN; (d) RF; (e) XGBoost; (f) LightGBM; (g) CatBoost; (h) ERT; (i) Voting.

Specifically, the ERT and voting models showed higher predictive accuracy on the testing dataset, achieving the lowest values for RMSE and MAE, and the R^2 value both reached 0.88. The XGBoost, LightGBM and CatBoost models exhibited slightly lower performance in comparison, with their RMSE, MAPE, MAE, and R^2 metrics not quite matching those of the ERT and LightGBM models.

Furthermore, it can be observed that among the eight individual machine learning models, the five models demonstrating superior performance are all tree-based models. This indicates that tree-based models are particularly well-suited for the multi-target regression task investigated in this study. In comparison, the MDN model exhibited relatively lower accuracy; however, its performance remains acceptable, achieving an R^2 of 0.78 on the test set, which is within 10% of the results obtained by the other models.

Fig. 11 presents a Taylor diagram (Taylor et al., 2012) that comprehensively evaluates the performance of nine ML models in predicting *MQ*, *MS*, and *FV* on the testing set. A Taylor diagram offers a graphical means to compare model predictions with observed data, where each of the differently colored dots corresponds to a specific predictive model. The model whose dot lies closest to the observation point (red pentagram) indicates the highest level of prediction accuracy. As shown in Fig. 11(a) and Fig. 11(b), the voting model has the smallest distance to the observation point, indicating it is the optimal model for predicting *MQ* and *MS*. Similarly, Fig. 11(c) shows that for *FV* prediction, the voting model's accuracy is second only to the LightGBM model. Moreover, the voting model has the highest mean values of R^2 across all three prediction tasks (see Table B2), demonstrating the best predictive accuracy and generalization ability.

3.3. SHAP-based local interpretability

To illustrate the prediction process across the 9 machine learning models, a random instance was selected for detailed analysis. The feature values of this sample include *Pe* (0.1 mm) = 46, *Du* (cm) = 130, *SP* (°C) = 51, *AC* (wt.%) = 5, *AV* (%) = 4.17, *VMA* (%) = 16.9, *VFA* (%) = 75.34, *Ag2.36* (%) = 32.98, *Ag4.75* (%) = 42.91, *Ag9.5* (%) = 82.45, *FT* = Glass, *FC* (wt.%) = 0, *FL* (mm) = 0, *TS* (MPa) = 3100, *MT* (°C) = 850, and *MQ* (kN/mm) = 3.25. Fig. 12 shows SHAP force plots for *MQ* prediction of the selected sample, highlighting key features with concise information compared to the waterfall plot, where the base value represents the average prediction.

In Fig. 12, *AC* (5%) and *FT* (Glass) consistently contribute positively

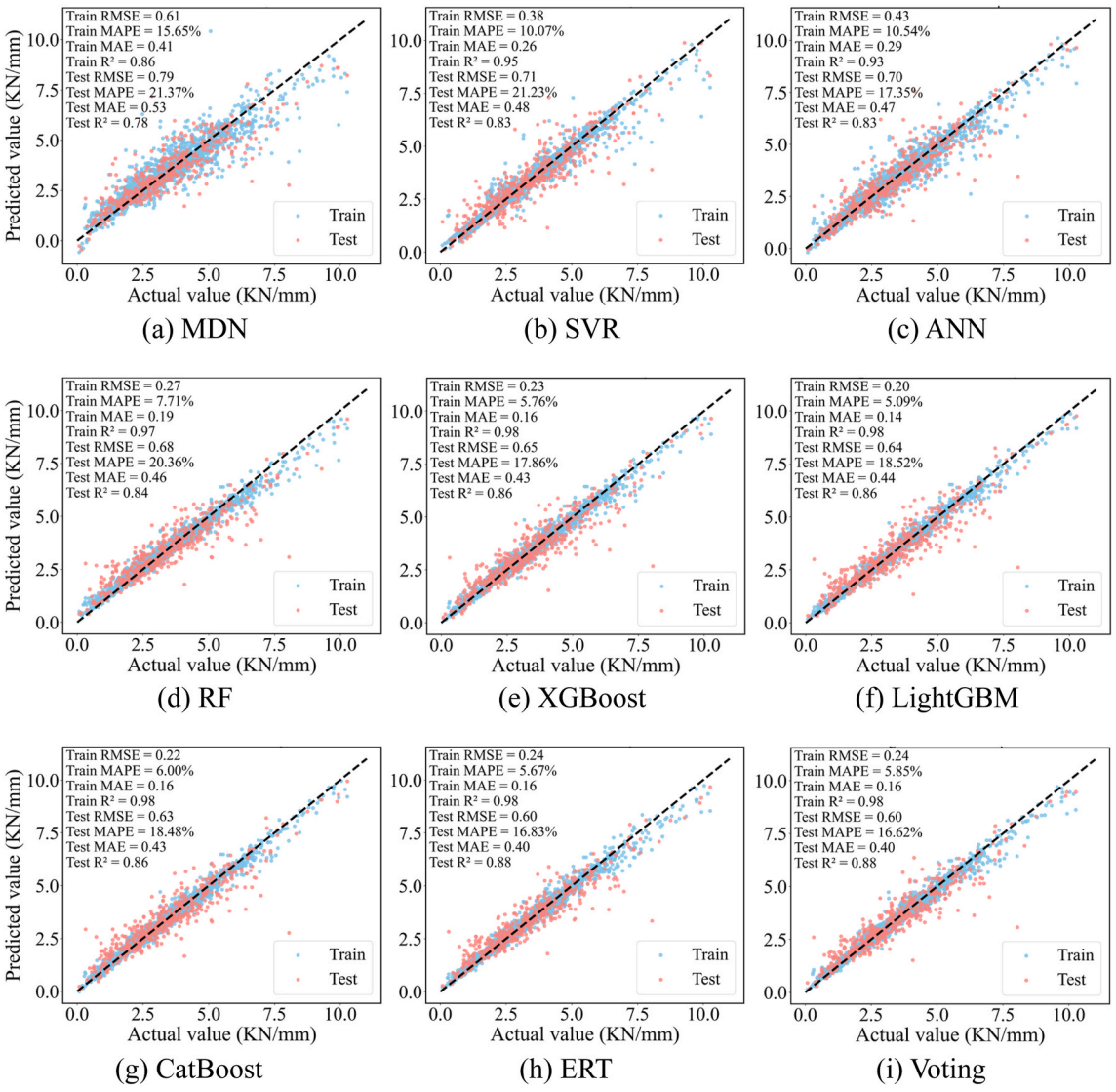

Fig. 10. Performance of ML models on training and testing with *MQ* as the prediction target: (a) MDN; (b) SVR; (c) ANN; (d) RF; (e) XGBoost; (f) LightGBM; (g) CatBoost; (h) ERT; (i) Voting.

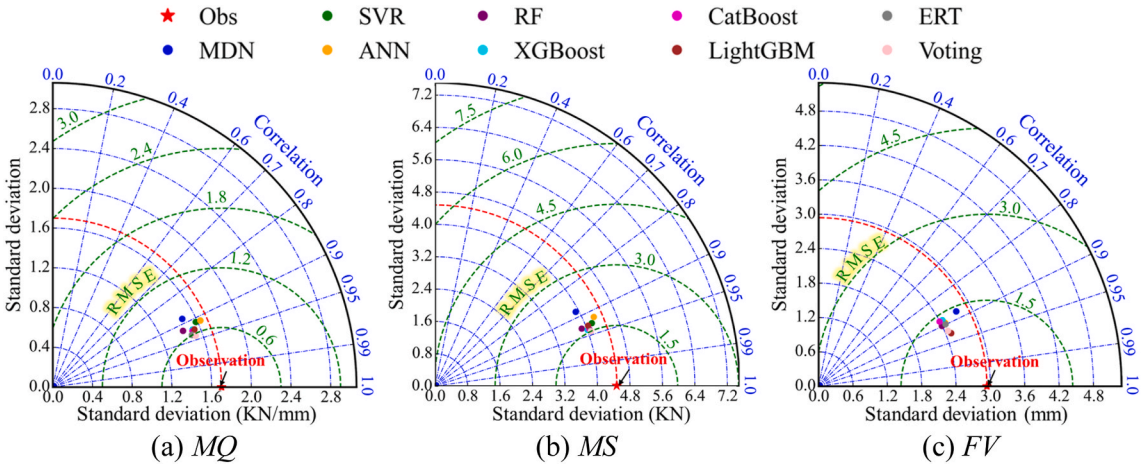

Fig. 11. Taylor diagram of the machine learning models for three outputs: (a) *MQ*; (b) *MS*; (c) *FV*.

to *MQ*, while *FC* (0%), *Ag9.5* (82.45%), and *MT* (850 °C) show negative contributions, lowering the predicted *MQ*. The final predicted *MQs* outputted by MDN, ANN, SVR, RF, XGBoost, LightGBM, CatBoost, ERT, and voting models are 3.47, 3.1, 3.35, 3.27, 3.21, 3.25, 3.29, 3.27, and

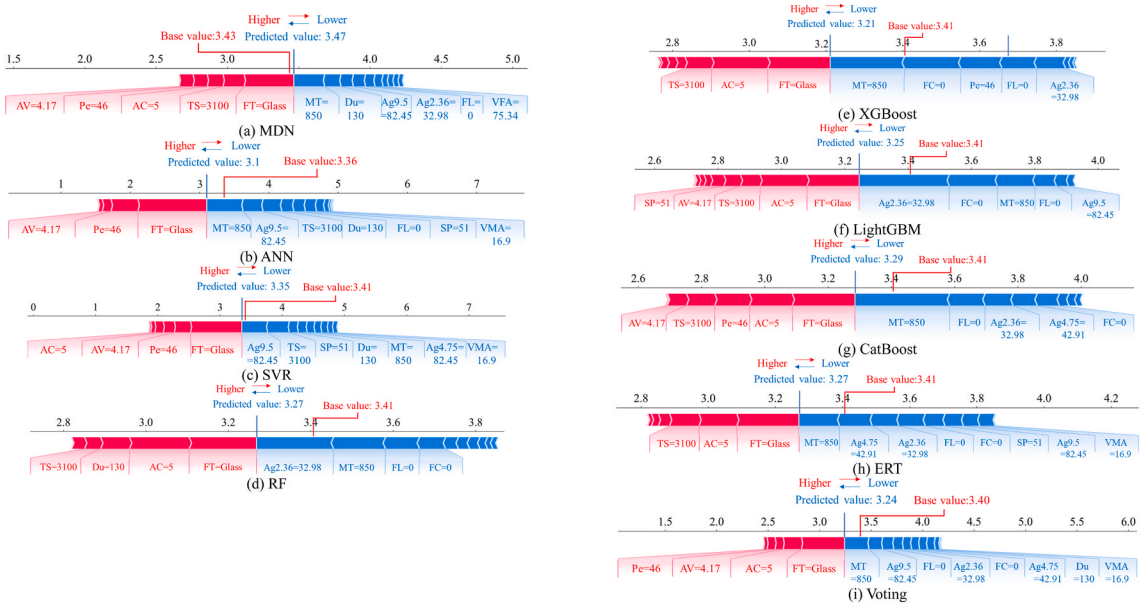

Fig. 12. Prediction process of nine machine learning models. Red bars indicate positive contributions, while blue bars indicate negative contributions. (For interpretation of the references to color in this figure legend, the reader is referred to the Web version of this article.)

3.24 kN/mm, respectively, resulting in relative errors between the actual *MQ* and the predictions are 6.77%, 4.62%, 3.08%, 0.62%, 1.23%, 0%, 1.23%, 0.62%, and 0.31% respectively. Except for the MDN model, the other eight models achieve prediction errors within 5%, confirming their effectiveness and precision.

3.4. SHAP-based global interpretability

3.4.1. Contribution of each feature

As discussed above, SHAP is capable to output the contribution of a special feature on the Marshall quotient (*MQ*) of FRAC in a sample, it can also calculate the contributions of all input features on output feature across all samples in the complete dataset. Fig. 13 displays SHAP-based interpretation of the outputs from voting model due to its superior performance, as noted previously. It includes pie charts illustrating the proportion of each feature's total impact based on the absolute magnitude of their SHAP values, and beeswarm plots displaying the distribution of SHAP values sorted by their magnitude. The beeswarm plots visualize the distribution of SHAP values for each feature, with dots representing samples colored by feature value (red for high feature value, blue for low feature value). Distance from the y-axis reflects the absolute SHAP value and impact, while features are ordered by average contribution. All models consistently identified the direction of feature influence. For instance, low *Pe* and *AC* values positively affect the output, whereas higher values reduce it.

The Beeswarm plots of other eight single models are shown in Fig. C1. As shown in the pie charts in Fig. 13 and Fig. C1, it is evident that eight of the nine models, excluding the ANN model, consistently identify *Pe* and *AC* as the two most influential features on the output. As shown in Table 3, both *Pe* and *AC* have an influence exceeding 10% and are classified as high-impact features. *FT*, *MT*, *TS*, *Ag2.36*, *SP*, *VMA*, *AV*, *FC*, and *Ag4.75*, with influences between 5% and 10%, are categorized as medium-impact features. *Du*, *FL*, *VFA*, and *Ag9.5*, with influences below 5%, are classified as low-impact features. On average, the 2 high-impact factors account for 27.06% of the influence, the 9 medium-impact factors 56.04%, and the 4 low-impact factors 16.86%.

3.4.2. Dependence analysis of each feature

To analyze the influence trends and threshold effects of critical features on the *MQ*, Fig. 14 presents the SHAP dependence plots for each input feature as generated by the voting model, which helps clarify the impact of each parameter on the *MQ* of FRAC.

According to Fig. 13, the top 11 input features (the 2 high-impact and 9 medium-impact ones) account for 83.1% of the total impact on the *MQ* of fiber asphalt concrete. Accordingly, SHAP dependence plots for these eleven critical features were fitted with Locally Weighted Scatterplot

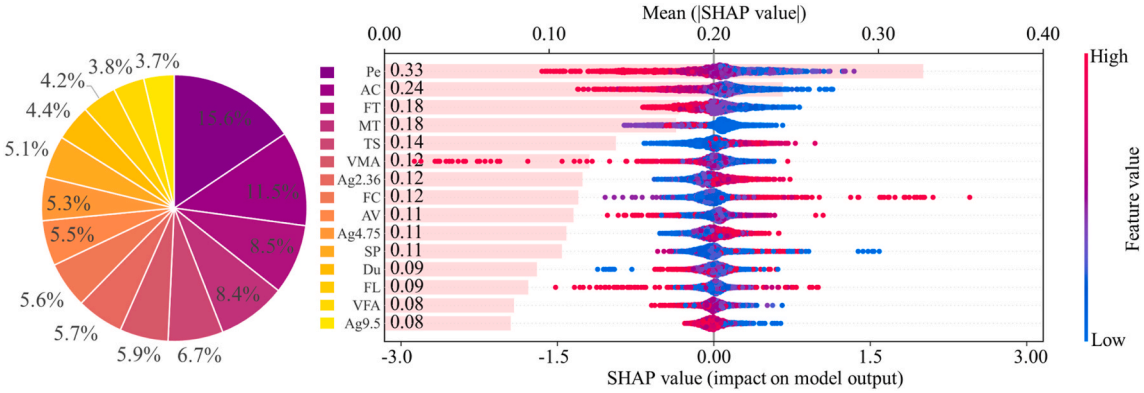

Fig. 13. SHAP-based interpretation of the outputs from voting model.

Table 3
Ranking the influence of features on predicting the Marshall Quotient (*MQ*) value.

Features	Percentage of models (%)									Average (%)
	MDN	ANN	SVR	RF	XGB	LGB	Cat	ERT	Voting	
Pe	12	14.4	12.9	19.9	16.4	16.9	15	17.6	15.6	15.63
AC	12.5	10.2	9.8	12.3	11.9	11.6	11.9	11.2	11.5	11.43
FT	9.7	10.7	8.1	6.7	6.2	5.6	5.8	6	8.5	7.48
MT	8.3	8.7	8.7	6.2	6.9	7.4	7.8	4.7	8.4	7.46
TS	8	5.1	6.3	7.5	6.6	7.3	6	6.4	6.7	6.66
Ag2.36	8.7	5.6	6.1	5.5	5.7	6.3	5.8	9.1	5.7	6.50
SP	3.5	5.3	4.9	6.8	8.2	7.8	6.5	7.6	5.1	6.19
VMA	4.3	6.8	5.5	4.9	6.2	6.4	7.4	4.7	5.9	5.79
AV	5.3	4	6.2	5.2	6	6.1	6.2	5.7	5.5	5.58
FC	4.3	4.1	5	4.9	6.3	6.7	6.3	4.6	5.6	5.31
Ag4.75	4.8	7.1	5.8	3.5	3.8	4.3	5.4	5.6	5.3	5.07
Du	5.6	5.2	5.9	4.2	4.2	3.6	4	4.1	4.4	4.58
FL	3.8	4	4.3	4.5	4.7	3.7	5.3	4.6	4.2	4.34
VFA	4.4	4	5.5	4.9	3.9	3.3	3.9	5	3.8	4.30
Ag9.5	4.7	4.7	5	2.9	2.9	3.1	2.6	3.2	3.7	3.64

Note:XGB denotes XGBoost; LGB indicates LightGBM; Cat refers to the CatBoost.

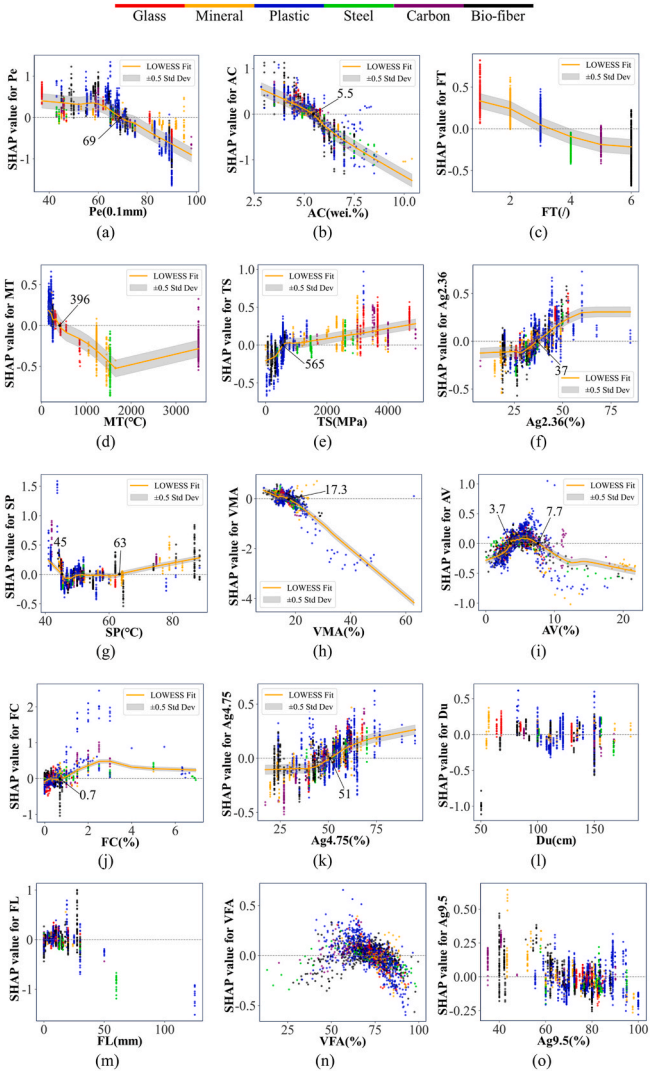

Fig. 14. SHAP dependence plots for fifteen input variables based on voting model with *MQ* as the prediction target: (a) *Pe*; (b) *AC*; (c) *FT*; (d) *MT*; (e) *TS*; (f) *Ag2.36*; (g) *SP*; (h) *VMA*; (i) *AV*; (j) *FC*; (k) *Ag4.75*; (l) *Du*; (m) *FL*; (n) *VFA*; (o) *Ag9.5*. (Note: Dot colors indicate six fiber categories, as shown in the color bar). (For interpretation of the references to color in this figure legend, the reader is referred to the Web version of this article.)

Smoothing (LOWESS) curves and visualized alongside the corresponding ±0.5 standard deviation error bands to quantify uncertainty. This approach allows for parametric analysis by investigating the relationship between the parameter values and their respective SHAP values. In contrast, the cumulative impact of the other four low-impact features (*Du*, *FL*, *VFA*, and *Ag9.5*) is negligible (16.86% of the total impact). Thus, these four parameters are excluded from further analysis. The dots in the plots are color-coded according to the six fiber types outlined in Table 1: Red for glass fiber, orange for mineral fiber, blue for plastic fiber, green for steel fiber, purple for carbon fiber, and black for bio-fiber.

When the baseline *MQ* value is 3.40 (see Fig. 12(i)), Figs. 14(a) and (b) show that for the two high-impact features, the SHAP values corresponding to the *Pe* and *AC* gradually become negative with their increase, indicating a negative correlation with the Marshall quotient of FRAC. Thus, *Pe* values below 69 (in 0.1 mm units) and *AC* values below 5.5% can help increase the *MQ*. Furthermore, analysis of the nine medium-impact characteristics reveals: Firstly, as illustrated in Fig. 14 (c), glass fiber, mineral fiber, and plastic fiber all exhibit positive effects on *MQ*. Among the remaining eight characteristics (Fig. 14(d) to 14(k)), *TS*, *Ag2.36*, *FC*, and *Ag4.75* demonstrate positive correlations with *MQ*, and *MT* and *VMA* show negative correlations. While *SP* and *AV* display alternating positive and negative correlations with *MQ*. Based on these relationships, the following thresholds are recommended to enhance *MQ* performance: $MT < 396$ °C, $TS > 565$ MPa, $Ag2.36 > 37\%$, $SP < 45$ °C or $SP > 63$ °C, $VMA < 17.3\%$, $3.7\% < AV < 7.7\%$, $FC > 0.7\%$, $Ag4.75 > 51\%$.

3.5. Pairwise interaction analysis based on causal inference

As shown in Fig. 15, DAG constructed using the LiNGAM algorithm reveals causal interactions among 15 black input variables and 3 red output variables. The analysis highlights several significant causal chains within the input space; for instance, *Pe* exerts a negative direct effect on *SP* (−0.34), which in turn positively influences *AV* (+0.28). Concurrently, *AC* positively modulates *VFA* (6.32), and the resulting *VFA* reduction propagates to suppress *FV* (−0.40). Ultimately, this *FV* decrement feeds back to impair *MQ* (−0.32). The DAG also uncovers variables that operate through both direct and indirect pathways. Notably, *Ag4.75* emerges as a pivotal driver, influencing output responses via routes such as *Ag4.75→FC→Ag9.5→MS* and *Ag4.75→Ag9.5→MS* (indirect), while also exerting direct effects on *MS* (+0.54) and *MQ* (−0.74). These multi-pathway effects establish *Ag4.75* as a key determinant of performance outcomes. Overall, the DAG not only confirms the direction and magnitude of effects identified through SHAP analysis but also exposes hidden indirect pathways that link input features to performance metrics, thereby offering a deeper

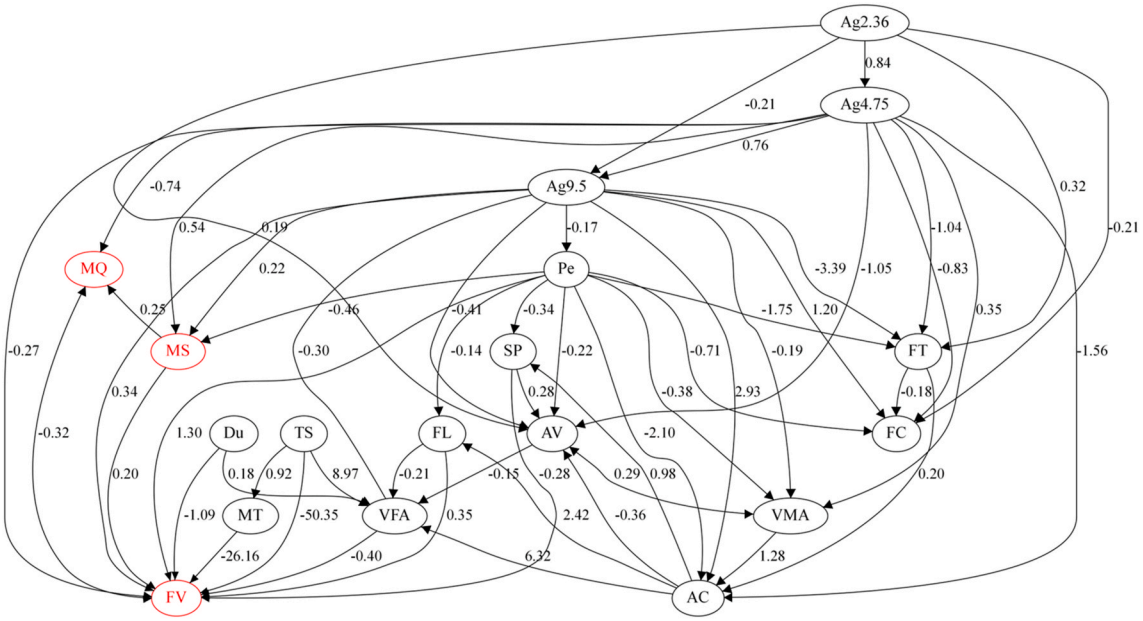

Fig. 15. Causal inference pathways for 15 input features and 3 output features. (Note: The red circles represent 3 output features). (For interpretation of the references to color in this figure legend, the reader is referred to the Web version of this article.)

understanding of the causal structure underlying FRAC behavior.

3.6. Life cycle assessment and design recommendations

3.6.1. Economy and environmental impacts

Inventory data for each raw material are collected, covering unit cost (USD), carbon emissions (kg), and embodied energy (MJ) to produce 1 kg raw materials, as shown in Table D1. The raw materials considered include asphalt, coarse aggregate, fine aggregate, filler, and fiber. Fig. 16 plots the distribution of inventory data.

The average of the range values of each raw material was adopted in the calculation, as shown in Table 4. It outlines the cost, carbon emission, and embodied energy associated with each raw material employed in the production of FRAC. These values are then normalized by the Marshall quotient to obtain normalized material cost, normalized carbon footprint, and normalized energy consumption metrics. This approach enables a meaningful comparison of FRAC mixtures in terms of both mechanical performance and environmental/economic impact.

3.6.2. Cost analysis

The total cost analysis of 2490 FRAC is shown in Fig. 17(a). Based on the LCA results, the cost of producing 1 kg of FRAC ranges from $0.064 to $0.82, with an average of $ 0.11. The majority of FRAC mixtures had a cost below $0.1 per kg, indicating that FRAC can be economically viable for large-scale construction applications when properly formulated.

Fig. 17(b) presents the *MQ*-normalized cost analysis of FRAC. The *MQ*-normalized cost, representing the expense to achieve 1 kN/mm of Marshall quotient, varies between $0.0073/(kN/mm) and $3.53/(kN/

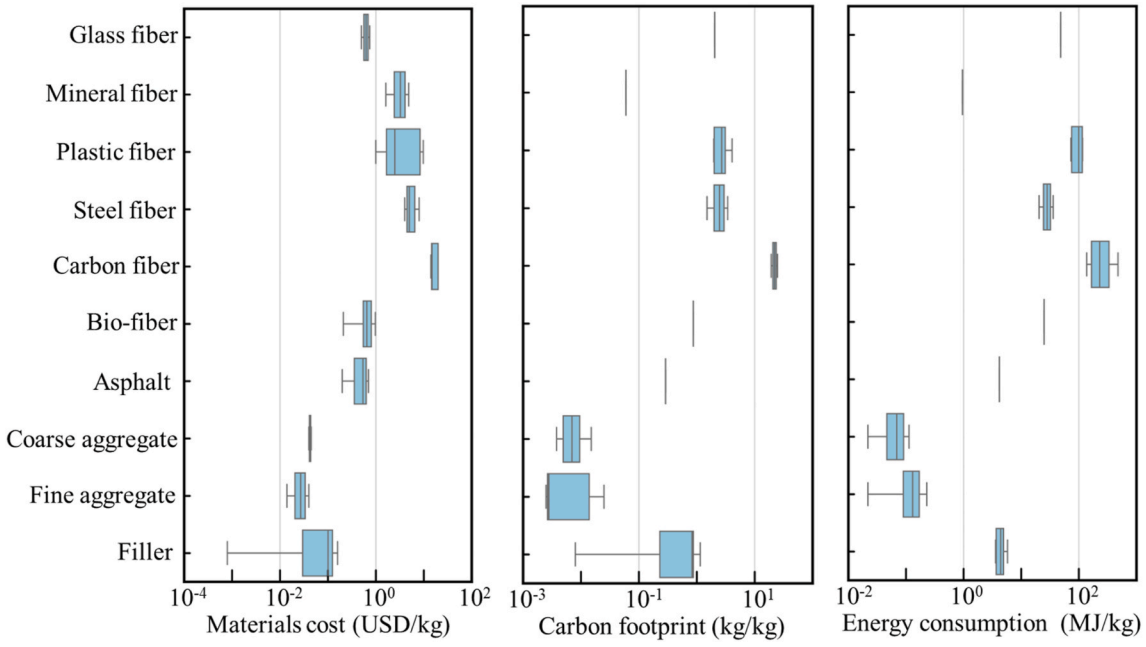

Fig. 16. Life-cycle carbon footprint, cost, and embodied energy of ingredients.

Table 4
Inventory data for each raw ingredient used in life cycle assessment.

No.	Materials		Cost ($/kg)	Carbon footprint (kg/kg)	Energy consumption (MJ/kg)
1	Fiber	Glass fiber	0.63	2.04	48.33
		Mineral fiber	3.25	0.06	0.96
		Plastic fiber	6.06	3.02	94.5
		Steel fiber	6	2.47	28.28
		Carbon fiber	24.55	22.06	307.4
		Bio-fiber	0.6	0.87	25
2	Asphalt		0.77	0.29	4.17
3	Coarse aggregate		0.043	0.0094	0.068
4	Fine aggregate		0.027	0.014	0.13
5	Filler		0.084	0.58	3.08

mm), with average value of $0.049/(kN/mm). Most FRAC mixtures had a *MQ*-normalized cost below $0.05/(kN/mm).

3.6.3. Carbon emission

Fig. 18(a) shows the total carbon emission analysis for 2490 FRAC mixtures. According to the LCA results, the carbon emission of producing 1 kg of FRAC ranges from 0.035 kg to 0.72 kg, with an average of 0.078 kg. Most mixtures carbon emission less than 0.08 kg per 1 kg. Fig. 18(b) presents the *MQ*-normalized carbon footprint for mixtures, indicating the carbon emissions required to achieve 1 kN/mm of Marshall quotient. This value ranges from 0.006 kg/(kN/mm) to 2.1 kg/(kN/mm), with an average of 0.034 kg/(kN/mm). Very low Marshall quotient, such as 0.08-0.15 kN/mm, lead to disproportionately high *MQ*-normalized carbon footprints, often exceeding 1 kg/(kN/mm). The majority of mixtures remained below 0.04 kg/(kN/mm), with the lowest carbon footprint recorded at 0.0058 kg/(kN/mm).

3.6.4. Energy efficiency

Fig. 19(a) presents the total energy consumption analysis for 2490 FRAC mixtures. Based on the LCA results, the energy required to produce 1 kg of FRAC ranges from 0.32 MJ to 9.69 MJ, with an average of 0.84 MJ. Most mixtures consume less than 0.9 MJ of material per kg. Fig. 19(b) shows the *MQ*-normalized energy consumption for mixtures, representing the energy needed to achieve 1 kN/mm of Marshall quotient. This metric ranges from 0.045 MJ/(kN/mm) to 44.87 MJ/(kN/mm), with an average of 0.4 MJ/(kN/mm). As with *MQ*-normalized carbon emissions, very low *MQ* (e.g., 0.08–0.15 kN/mm) result in disproportionately high energy consumption per unit strength, often exceeding 20 MJ/(kN/mm). The majority of mixtures fall below 0.35 MJ/(kN/mm), with the lowest recorded value at 0.045 MJ/(kN/mm).

3.6.5. Design recommendations

Fig. 20(a) illustrates the use of a 3D plot to identify the optimal FRAC mixture based on total cost, carbon emissions, and energy consumption. Each point in the plot represents a specific mix, allowing for a clear comparison across environmental and economic dimensions. By visualizing these three key performance indicators together, it becomes possible to detect trade-offs between cost-efficiency and sustainability. Mixtures with low values across all axes cluster near the origin, and the optimal design is highlighted as the point with the lowest combined impact. The optimal mixture, selected based on minimizing total cost, carbon emissions, and energy consumption, yields $0.068 in cost, 0.036 kg of CO_2 emissions, and 0.32 MJ of energy use per kg. This mixture consists of 32.02% with fine aggregate, 61.56% with coarse aggregate, 2.42% with filler and 4% with asphalt, with no fiber included. The optimal mixture exhibits a *MS* of 9.7 kN, a *FV* of 2.39 mm, and a *MQ* of 4.06 kN/mm, demonstrating robust mechanical performance that meets typical construction standards.

Fig. 20(b) presents a 3D plot of the *MQ*-normalized cost, carbon emission, and energy consumption for each FRAC mixture. The optimal FRAC mixture achieves a cost of $0.007 per kN/mm, a carbon emission of 0.006 kg per kN/mm, and an energy consumption of 0.045 MJ per kN/mm. This mixture consists of 29.12% of fine aggregate, 60.1% of coarse aggregate, 6.11% of filler, 4.67% of asphalt, with no fiber included. It delivers a *MS* of 16.85 kN, a *FV* of 1.65 mm, and a *MQ* of 10.18 kN/mm, indicating robust mechanical properties while minimizing environmental and economic impacts.

Finally, as shown in Fig. 20(a) and Fig. 20(b), asphalt concrete reinforced with plastic, steel, and carbon fibers has higher total cost, total carbon emissions and total embodied energy, and its *MQ*-normalized performance is poor. Thus, these fibers contribute little to asphalt concrete properties. Hence, from economic, environmental and performance perspectives, glass, mineral, and bio-fibers are better asphalt

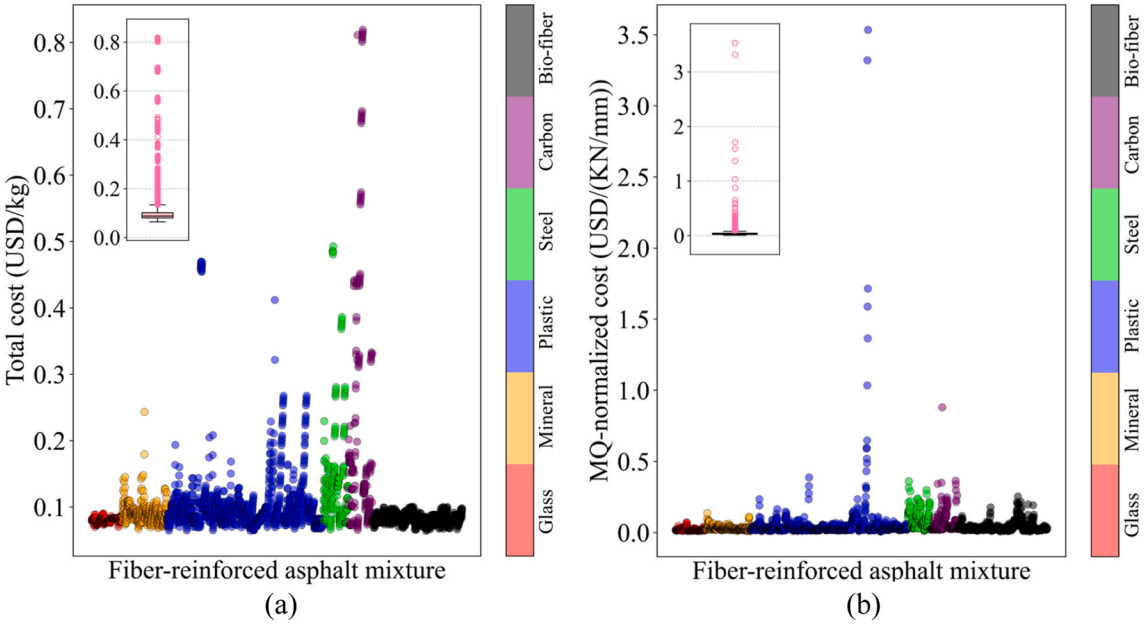

Fig. 17. Cost analysis of FRAC: (a) total cost; (b) *MQ*-normalized cost.

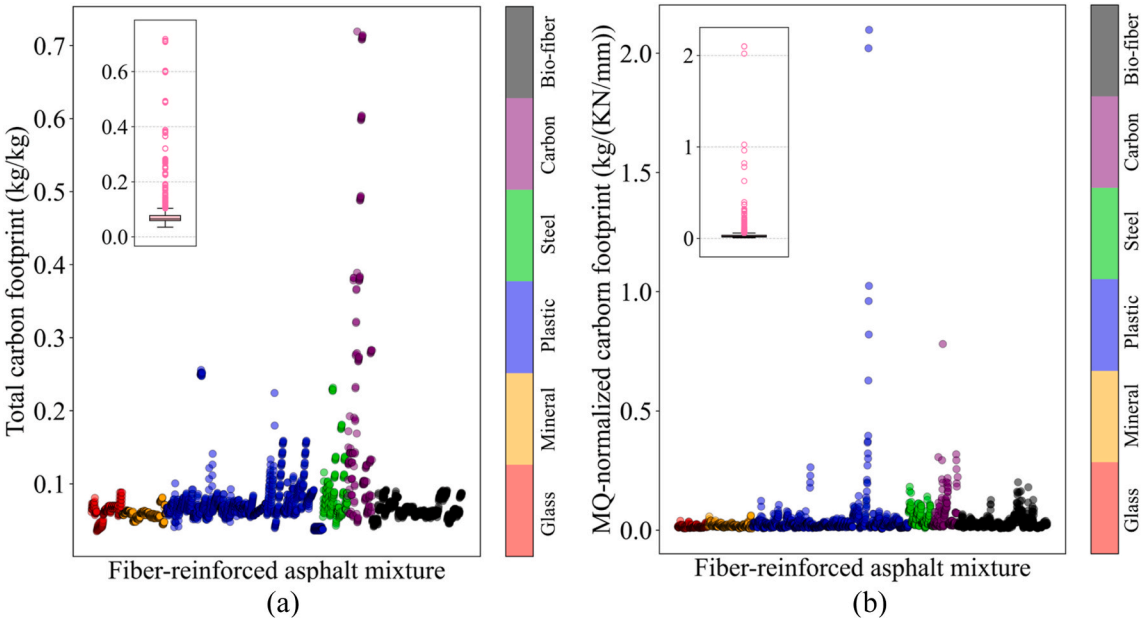

Fig. 18. Carbon analysis of FRAC: (a) total carbon emission; (b) *MQ*-normalized carbon emission.

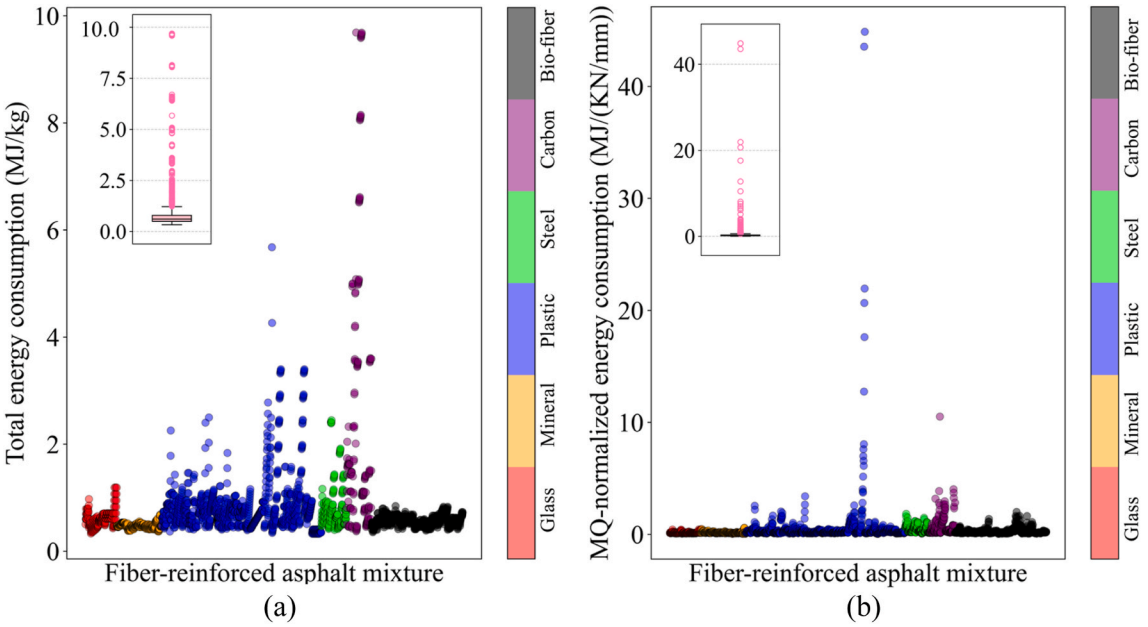

Fig. 19. Energy consumption analysis of various FRAC: (a) total energy consumption; (b) *MQ*-normalized energy consumption.

concrete fiber additives.

3.7. Discussions

To examine whether incorporating fibers leads to systematic sustainability differences at the dataset level, the samples were divided into seven groups according to fiber content: mixtures with $FC = 0$ were treated as conventional asphalt concrete (AC), while mixtures with $FC \neq 0$ were further classified as six FRAC subgroups according to fiber type. Fig. 21 compares AC with these FRAC subgroups using boxplots of total cost, total carbon footprint, and total energy consumption, as well as their *MQ*-normalized counterparts (GF = Glass FRAC; MF = Mineral FRAC; BF = Bio-FRAC; PF = Plastic FRAC; CF = Carbon FRAC; SF = Steel FRAC).

The results indicate that sustainability performance of FRAC is highly dependent on fiber type. In the total indicators (Fig. 21(a)–Fig. 21(c)), CF and PF generally show higher central tendencies and broader distributions than AC, SF tends to fall in an intermediate range, whereas GF, MF, and BF remain closer to AC with comparatively moderate dispersion. More importantly, the *MQ*-normalized results (Fig. 21(d)–Fig. 21(f)) clarify which fiber additives deliver the best impact–performance efficiency. Among the six subgroups, glass fiber (GF) stands out as the optimal additive because its *MQ*-normalized cost (0.02 vs. 0.03 USD/(kN/mm)), carbon footprint (0.015 vs. 0.022 kg/(kN/mm)), and energy consumption (0.156 vs. 0.181 MJ/(kN/mm)) are all lower than those of conventional asphalt concrete, with corresponding reductions of 33%, 32%, and 14%, respectively. This demonstrates that reinforcement with glass fiber can simultaneously improve mechanical performance and enhance environmental efficiency on an "impact per unit MQ" basis.

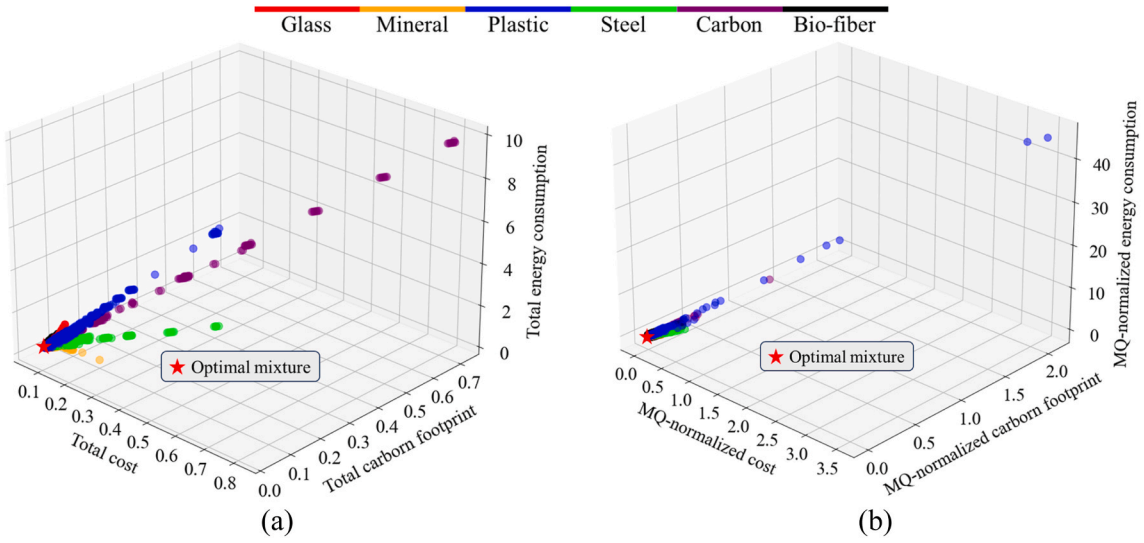

Fig. 20. Evaluation of optimal design based on: (a) total cost, carbon emission, and energy consumption for each mixture; (b) *MQ*-normalized cost, carbon emission, and energy consumption for each mixture.

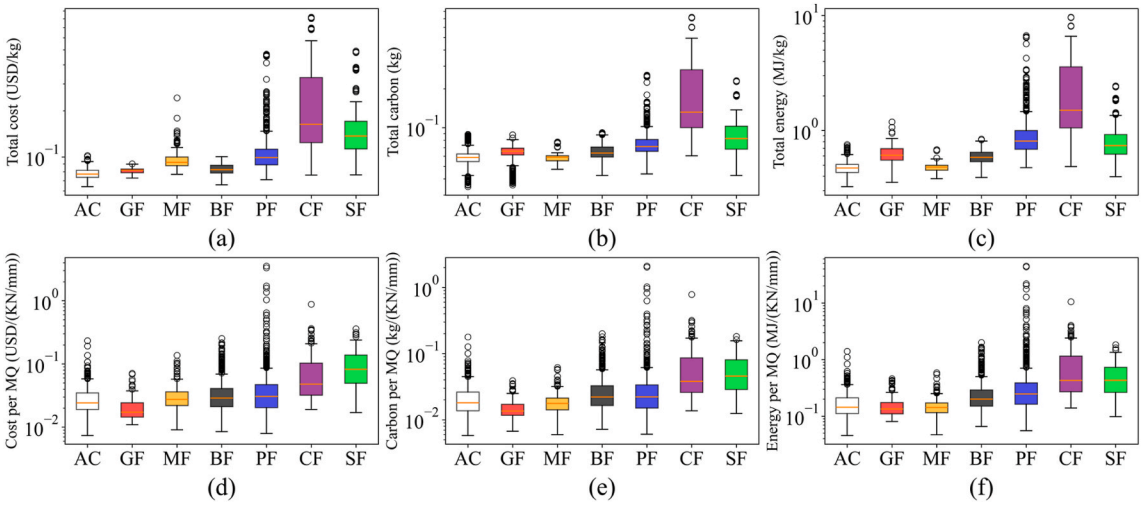

Fig. 21. Comparison of AC and FRAC subgroups in terms of: (a) total cost; (b) total carbon footprint; (c) total energy consumption; (d) MQ-normalized cost; (e) MQ-normalized carbon footprint; (f) MQ-normalized energy consumption. (Note: GF = Glass FRAC; MF = Mineral FRAC; BF = Bio-FRAC; PF = Plastic FRAC; CF = Carbon FRAC; SF = Steel FRAC).

In summary, the comparison supports the key engineering implication that fiber-reinforced mixtures are not only performance-enhancing materials, but can also be sustainability-improving systems when the appropriate fiber type is selected.

4. Graphic user interface platform

The GUI platform was developed using the Streamlit framework in Python (see Fig. 22). It allows users to input 15 parameters related to asphalt, aggregate, and fiber properties. Firstly, entering the parameters and clicking the prediction button, the system can predict three key performance indicators of the asphalt mixture: *MQ, MS*, and *FV* using pre-trained models. Secondly, the platform also provides SHAP analysis, displaying force plots and waterfall plots to show how each input parameter affects the three predicted results, making the model's decision-making process more understandable. Finally, the system is embedded with an LCA module, which automatically calculates the proportion of asphalt, fibers, coarse and fine aggregates, and fillers in the mixture based on input parameters. Combined with the unit cost, carbon footprint, and energy consumption database of each component, it quantitatively analyzes the total life cycle cost, carbon emissions, and energy consumption of the mixture. Meanwhile, the multi-dimensional collaborative evaluation of performance, environment and economy is achieved through *MQ*-normalized processing. The platform is available at https://frac-properties-prediction-system-nppcfabhqmyhgwzcfnv8oe.streamlit.app/.

5. Limitations and future research

This study offers an integrated, data-driven framework that combines machine learning prediction, feature importance analysis, and life cycle assessment to support sustainability-oriented FRAC design. By identifying the key design variables governing performance and quantifying their associated environmental and economic impacts, the findings enable more informed selection and optimization of mixture parameters, especially fiber type and content, rather than treating fiber addition as universal benefits.

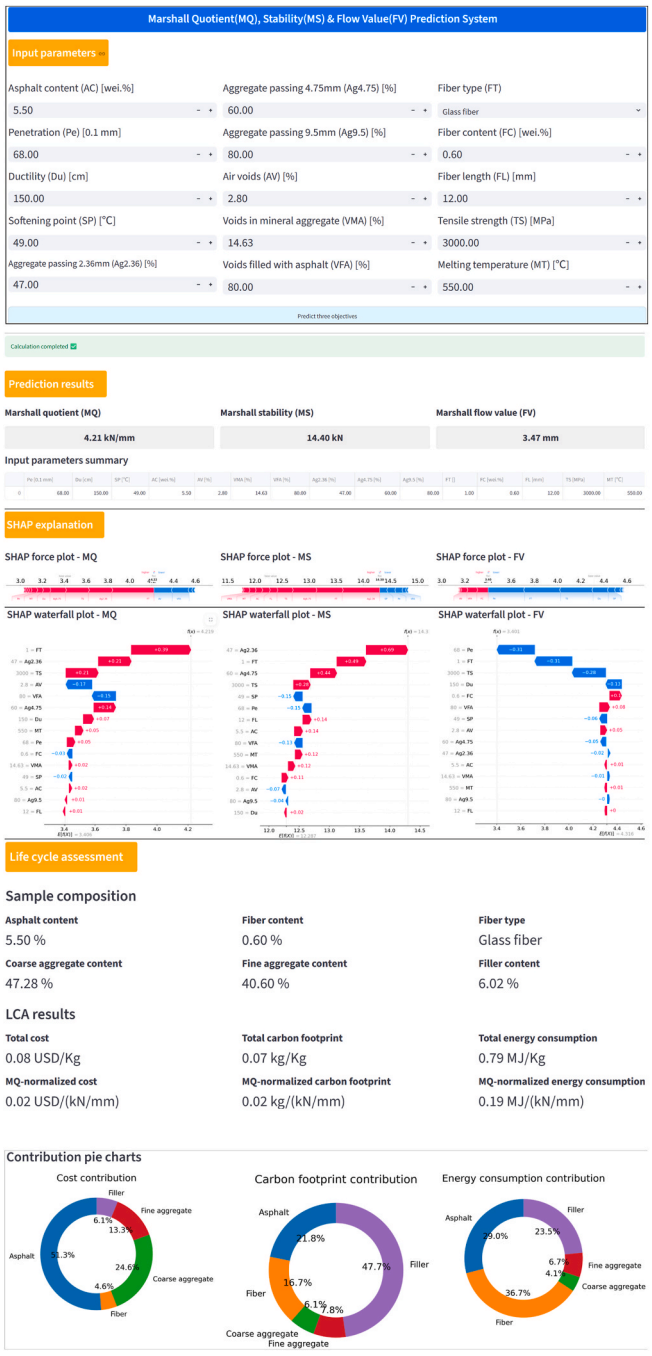

Fig. 22. GUI example for predicting the mechanical and sustainable performances of FRAC.

5.1. Limitations of this study

This study provides a data-driven basis for sustainability-oriented FRAC design by jointly examining mechanical performance and material-level LCA indicators. The results show that the sustainability impacts of fiber incorporation are highly dependent on fiber type and content, and therefore FRAC mix design should be guided by an integrated mechanical performance-LCA framework rather than assuming that adding fibers is universally beneficial to asphalt concrete.

The dataset in this study was compiled from a broad range of published sources, which inevitably introduced inconsistencies in key dimensions such as asphalt and aggregate types, fiber composition, geographic origin, and reporting format. These variations may affect the reliability and comparability of performance evaluation, thereby limiting the generalizability of the findings.

Moreover, the current LCA is confined to a cradle-to-gate scope at the material level, while the practical LCA application of FRAC in road and hydraulic engineering remains limited. Previous studies on asphalt pavement systems have demonstrated the importance of incorporating full life-cycle cost with maintenance stage into sustainability assessments (Ma et al., 2023; Zhang et al., 2023; Jin et al., 2022b; Wu et al., 2024).

5.2. Opportunities for future research

Future studies should prioritize establishing a standardized and region-specific FRAC database with consistent material characterization and experimental protocols to improve reproducibility, robustness, and interpretability in data-driven evaluations. Building on a stronger data foundation, this framework can be extended from a cradle-to-gate scope to a cradle-to-grave perspective by incorporating real engineering case studies that cover construction, transportation, compaction, service life, and maintenance stages. In parallel, integrating high-dimensional and multi-source datasets from both lab testing and field monitoring will enhance model robustness and practical relevance, thereby supporting more reliable and sustainable FRAC design decisions.

As the database continues to grow, the predictive models embedded in the GUI platform should be periodically retrained and updated to improve generalization and keep the system accurate over time. Ultimately, the long-term goal is to develop an open, continuously evolving platform that reflects the latest data and methodological advances, increasing its accessibility and usefulness for both research and engineering applications.

6. Conclusion

This research employed nine machine learning algorithms to predict the Marshall stability, flow value, and Marshall quotient of FRAC. This study compiled a dataset, comprising six categories of fibers, containing 2490 samples and 18 variables, designated for training and evaluating machine learning models. To evaluate the performance of the machine learning models, four metrics MAE, MAPE, RMSE, and R^2 were employed. Additionally, the SHAP and LiNGAM methods were used to explain prediction mechanisms and conduct parameter analysis. Finally, a cradle-to-gate LCA was performed to evaluate the economic and environmental impacts of FRAC, and optimal design recommendations were provided. Based on the aforementioned analysis, the following conclusions are drawn:

- Except for MDN, the other eight machine learning models have high prediction accuracy for the *MS*, *FV* and *MQ* of FRAC. Their R^2 on the test dataset exceeds 0.83, and their prediction error for randomly sampled sample is less than 5%. The voting model performed the best. Its average R^2 for predicting *MS*, *FV*, and *MQ* of FRAC on the test dataset reached 0.87, showing high robustness and strong generalization.
- SHAP analysis indicated that the *Pe* and *AC* were the two most influential features on *MQ*, with their combined contribution exceeding 27%. Subsequently, the *FT*, *MT*, *TS*, *Ag2.36*, *SP*, *VMA*, *AV*, *FC*, and *Ag4.75* were classified as medium-impact variables. Conversely, *Du*, *FL*, *VFA*, and *Ag9.5* were consistently identified as low-impact variables. On average, medium-impact features contributed 56.04% to the model predictions, while low-impact features accounted for merely 16.86% of the total influence.
- *Pe, AC, MT,* and *VMA* are negatively correlated with *MQ. TS, Ag2.36, FC,* and *Ag4.75* are positively correlated with *MQ. SP* and *AV* show alternate positive and negative correlations with *MQ.* To enhance *MQ*, the following parameter settings are recommended: *Pe* $<$ 69 dmm, *AC* $<$ 5.5%, *MT* $<$ 396 °C, *TS* $>$ 565 MPa, *Ag2.36* $>$ 37%, *SP* $<$

45 °C or $SP > 63$ °C, $VMA < 17.3\%$, $3.7\% < AV < 7.7\%$, $FC > 0.7\%$, $Ag4.75 > 51\%$.

- Based on the LCA and XAI analyses, among the six fiber additives, the inclusion of steel fiber and carbon fiber tended to increase the production cost, carbon emissions, and energy consumption of FRAC, while offering relatively limited performance benefits within the scope of this study. Plastic fiber and bio-fiber also showed comparatively less favorable outcomes in terms of environmental impact and mechanical enhancement, respectively. In contrast, glass fiber and mineral fiber provided more balanced mechanical-sustainable performance trade-offs, and glass fiber emerged as the optimal option: after *MQ*-normalization, glass FRAC achieved lower cost (0.02 vs. 0.03 USD/(kN/mm)), lower carbon footprint (0.015 vs. 0.022 kg/(kN/mm)), and lower energy consumption (0.156 vs. 0.181 MJ/(kN/mm)) than conventional asphalt concrete, indicating that glass fiber can simultaneously enhance mechanical and sustainable performance on an "impact per unit MQ" basis. Therefore, in the present dataset, glass fiber can be regarded as the most promising additive for achieving an optimal balance between mechanical performance and sustainability, with mineral fiber remaining a competitive alternative.
- Future research will focus on improving data consistency and expanding the analytical scope of this study. Building a standardized and region-specific FRAC database with unified material characterization and testing protocols will enhance the reliability and reproducibility of model-driven evaluations. In addition, extending the current cradle-to-gate LCA to a framework that incorporates real engineering processes (e.g. construction, transportation, service life, and maintenance) will provide a more comprehensive understanding of the environmental and economic implications of FRAC applications.

CRediT authorship contribution statement

Xiao Tan: Writing – review & editing, Writing – original draft, Supervision, Project administration, Methodology, Funding acquisition, Conceptualization. **Jianglei Xing:** Visualization, Software, Investigation, Formal analysis, Data curation. **Soroush Mahjoubi:** Writing – review & editing, Writing – original draft, Validation, Investigation. **Pengwei Guo:** Writing – review & editing, Project administration, Methodology, Investigation, Data curation. **Ziyao Wei:** Writing – original draft, Methodology, Conceptualization. **Yuan Wang:** Writing – review & editing, Project administration, Funding acquisition. **Jie Ren:** Validation, Project administration, Funding acquisition. **Li Ai:** Writing – review & editing, Validation, Project administration, Data curation. **Weina Meng:** Writing – review & editing, Validation. **Yi Bao:** Writing – review & editing, Validation.

Ethical approval

The results/data/figures in this manuscript have not been published elsewhere, nor are they under consideration by another publisher.

Declaration of competing interest

The authors declare the following financial interests/personal relationships which may be considered as potential competing interests: Xiao Tan reports financial support was provided by National Natural Science Foundation of China (Grant No: 52508343), Basic Research Program of Jiangsu (Grant No: BK20251486), and Fundamental Research Funds for the Central Universities (Grant No: B250201004).

Yuan Wang reports financial support was provided by National Natural Science Foundation of China (Grant No: U23B20144).

Ren Jie reports financial support was provided by National Natural Science Foundation of China (Grant No: 52209129).

Acknowledgement

The authors are grateful for the financial support provided by the National Natural Science Foundation of China (Grant No: 52508343, U23B20144, 52209129), Basic Research Program of Jiangsu (Grant No: BK20251486), and Fundamental Research Funds for the Central Universities (Grant No: B250201004).

Appendix A. Dataset description

Table A1
Summary statistics of fiber types and their corresponding quantities

Fiber categories	Fiber types	Number of samples
Glass fiber	Glass	206
Steel fiber	Steel	166
Carbon fiber	Carbon	165
Mineral fiber	Asbestos	24
	Basalt	233
	Calcium sulfate whisker	5
	Ceramic	14
	Mineral	2
	Parafibre	10
	Rock wool	10
Plastic fiber	Acrylic	4
	Aramid pulp	3
	Ecofibra	3
	Nylon	42
	Plastic	24
	Poly-acrylic	12
	Polyacrylonitrile	63
	Polyester	315
	Polyethylene	34
	Polyethylene terephthalate	90
	Polyparaphenylene terephtalamide	16

(*continued on next page*)

Table A1 (*continued*)

Fiber categories	Fiber types	Number of samples
	Polypropylene	381
	Textil	5
	Waste polyethylene terephthalate	46
	Waste polypropylene	8
Bio-fiber	Bamboo	14
	Banana	5
	Cellulose	25
	Chicken feather	30
	Coconut	73
	Coconut coir	15
	Coir	104
	Corn stalk	4
	Lignin	108
	Lignin + bamboo	4
	Palm	34
	Palm oil	10
	Rice straw	4
	Sisal	164
	Sugarcane bagasse	4
	Wood	5
	Xylogen	6

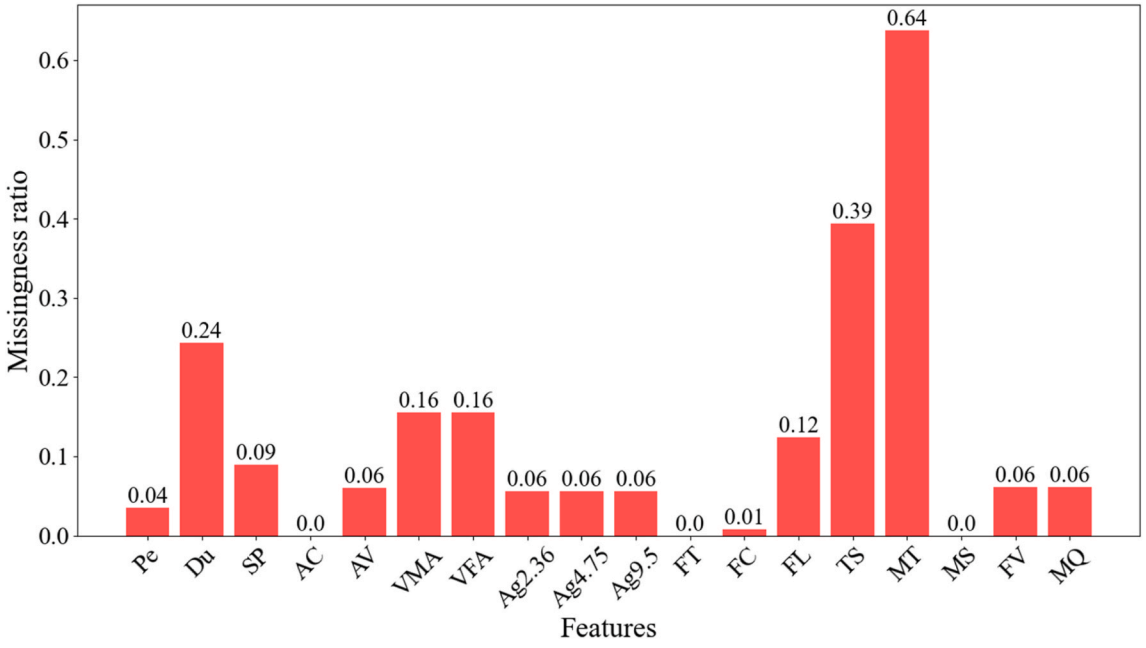

Fig. A1. Missingness ratio for fifteen input features and three output features.

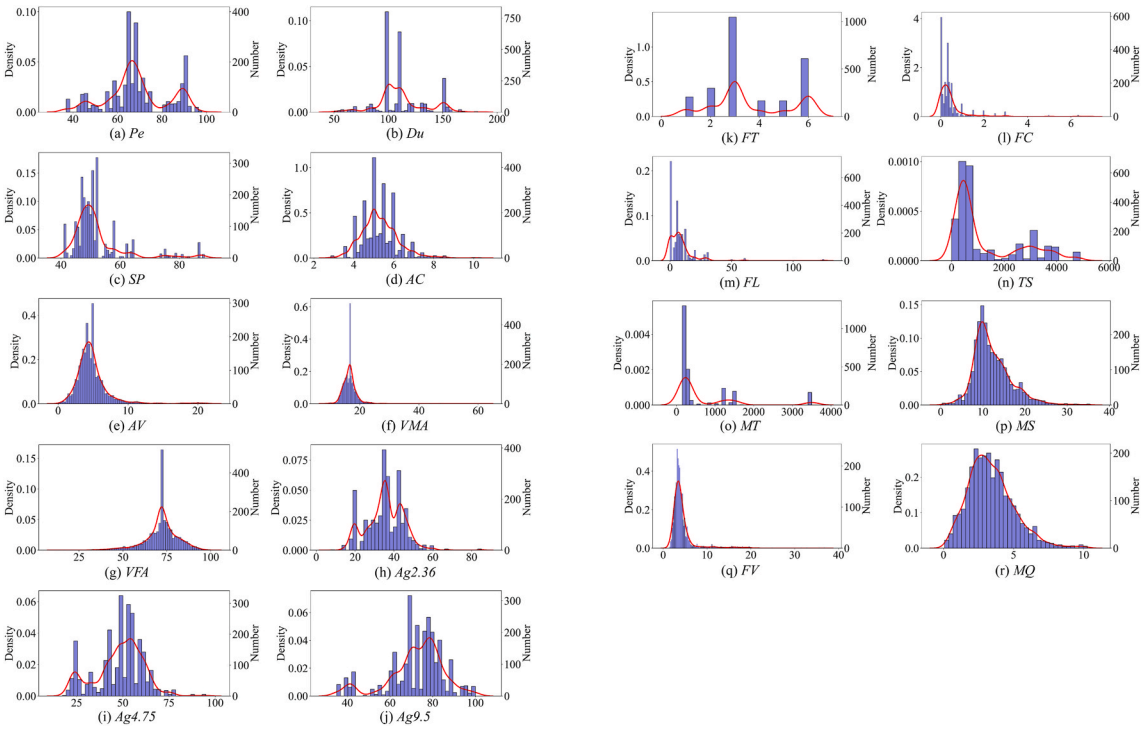

Fig. A2. Distribution of fifteen input features and three output features of FRAC: (a) *Pe*; (b) *Du*; (c) *SP*; (d) *AC*; (e) *AV*; (f) *VMA*; (g) *VFA*; (h) *Ag2.36*; (i) *Ag4.75*; (j) *Ag9.5*; (k) *FT*; (l) *FC*; (m) *FL*; (n) *TS*; (o) *MT*; (p) *MS*; (q) *FV*; (r) *MQ*.

Appendix B. Model performance demonstration

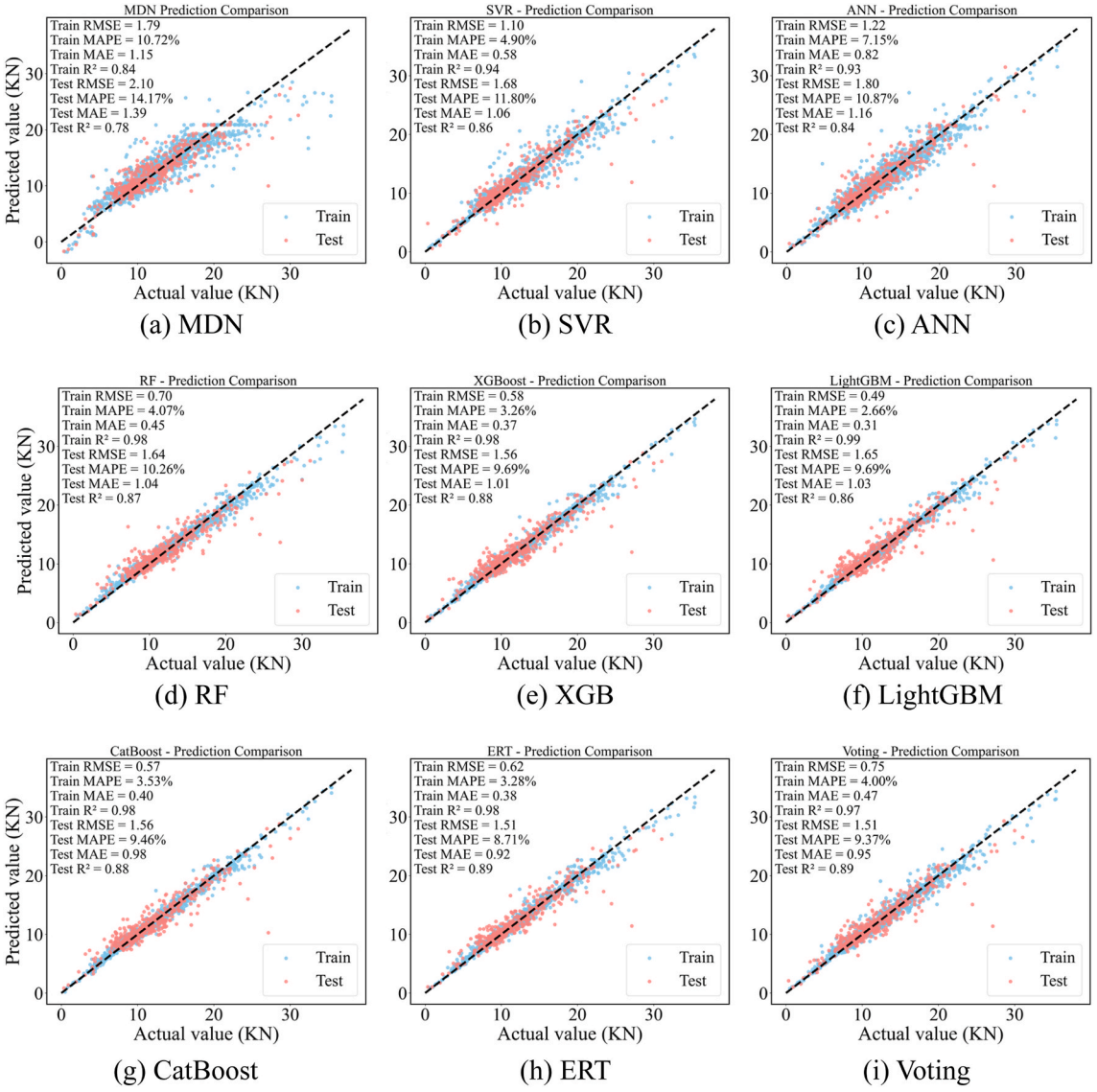

Fig. B1. Performance of ML models on training and testing dataset with *MS* as the prediction target: (a) MDN; (b) SVR; (c) ANN; (d) RF; (e) XGB; (f) LightGBM; (g) CatBoost; (h) ERT; (i) Voting.

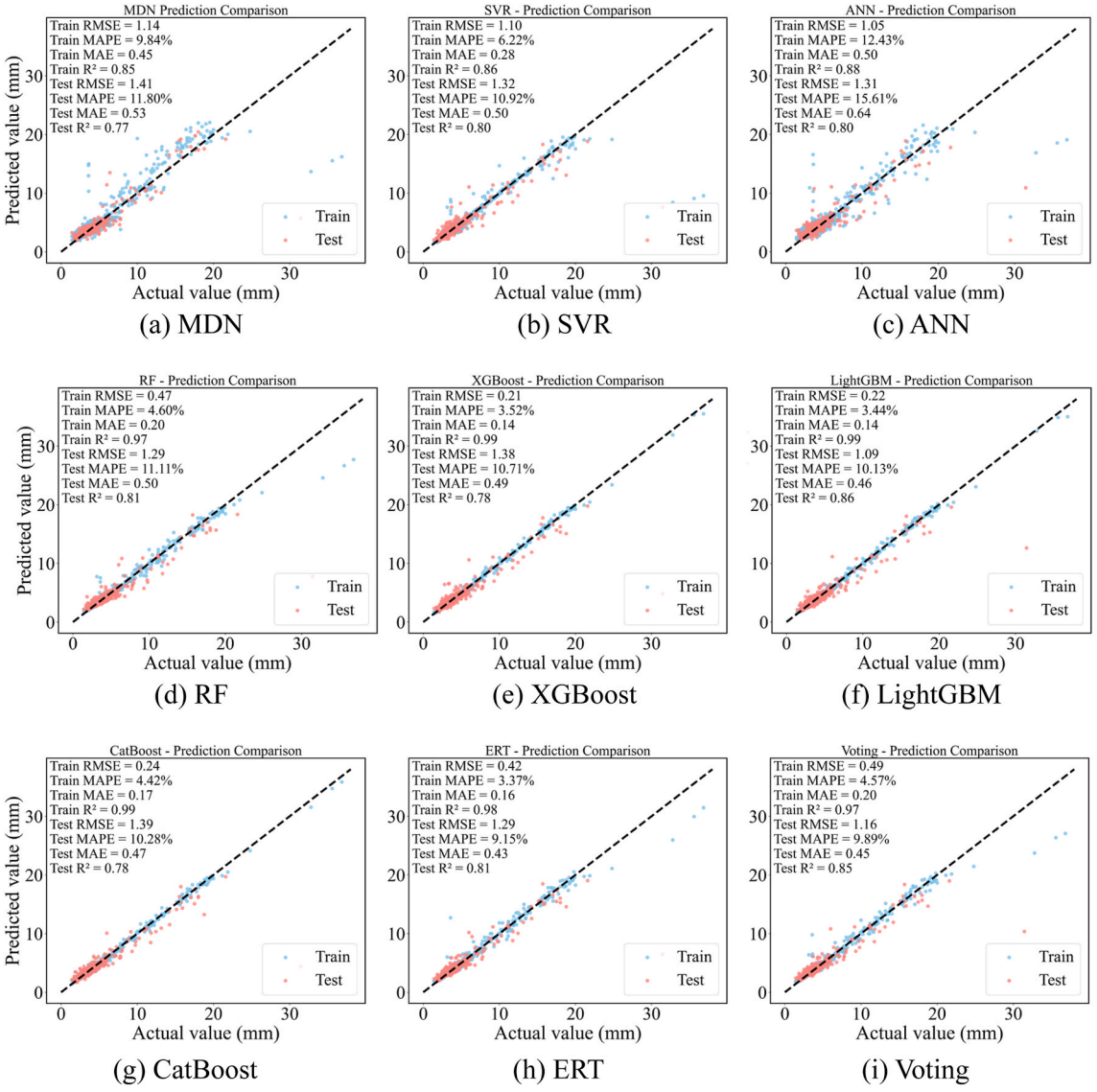

Fig. B2. Performance of ML models on training and testing dataset with *FV* as the prediction target: (a) MDN; (b) SVR; (c) ANN; (d) RF; (e) XGB; (f) LightGBM; (g) CatBoost; (h) ERT; (i) Voting.

Table B1
Optimal value of hyperparameter determined through NSGA-II

Algorithms	Hyperparameters	Descriptions
MDN	$d_1 = 512$	Number of neurons in the first hidden layer
	$d_2 = 256$	Number of neurons in the second hidden layer
	$d_3 = 128$	Number of neurons in the third hidden layer
	$d_4 = 64$	Number of neurons in the fourth hidden layer
	$d_5 = 32$	Number of neurons in the fifth hidden layer
	$n_c = 6$	Number of components in the mixture model
	$l_r = 0.0033$	Learning rate
	batch_size = 46	Batch size
	epochs = 100	Number of epochs
	es_patience = 48	Early stopping patience
	lr_patience = 8	Learning rate reduction patience
ANN	$n_{hl} = 4$	Number of the hidden layer
	n_e = (512, 256, 128, 64)	The number of neurons in the first to fourth hidden layers
	$l_r = 0.0003$	Learning rate
	$\alpha = 0.08$	Strength of the L2 regularization term
	Activation function: ReLU	ReLU function is used as the activation function
	max_iter = 1000	Maximum iterations
	Early_stopping = True	Activate the early stop mechanism

(*continued on next page*)

Table B1 (*continued*)

Algorithms	Hyperparameters	Descriptions
SVR	$C = 45$	Control model complexity
	$\gamma = 0.14$	Influences the scope of the kernel function
	$\varepsilon = 0.24$	Defines the tolerance range for errors
	kernel: RBF	RBF is adopted as the kernel function
RF	$n_e = 180$	Number of estimators
	$d_{\max} = 20$	Maximum depth of the tree
	$n_{\max} = 730$	Maximum number of leaf nodes
	$n_f = 7$	Limit number of features considered at each split
	Criterion: Squared error	Squared error is utilized to evaluate the splitting
XGBoost	$n_e = 540$	Number of estimators
	$l_r = 0.07$	Learning rate
	$d_{\max} = 6$	Maximum depth of each tree
	reg_alpha = 0.5	L1 regularization term coefficient
	reg_lambda = 13	L2 regularization term coefficient
LightGBM	$n_e = 440$	Number of estimators
	$l_r = 0.09$	Learning rate
	$d_{\max} = 19$	Maximum depth of the tree
	min_child_samples = 3	Minimum number of samples in a leaf node
	reg_alpha = 0.8	L1 regularization term coefficient
	reg_lambda = 25	L2 regularization term coefficient
	$n = 43$	Number of leaves
CatBoost	iterations = 1000	Number of iterations
	$d_{\max} = 7$	Maximum depth of the tree
	$l_r = 0.085$	Learning rate
	reg_lambda = 6	L2 regularization term coefficient
	criterion: RMSE	Root mean square error is used as the loss function
ERT	$n_e = 130$	Number of estimators
	$d_{\max} = 38$	Maximum depth of the tree
	$n_{\max} = 715$	Maximum number of leaf nodes
	$n_f = 12$	Limits the number of features considered at each split
	Min_samples_split = 5	Minimum number of samples required for node splitting
	Criterion: Squared error	Squared error is utilized to evaluate the splitting
Voting	$n_m = 4$	Number of base models
	Base_models = [ERT, LightGBM, ANN, SVR]	Four base models
	Weights = [0.33, 0.33, 0.17, 0.17]	Weights corresponding to the four base models

Table B2
Performance metrics of the models for FRAC properties on testing set

Performance metrics	Model	Output			Average
		MQ	MS	FV	
R^2	MDN	0.78	0.78	0.77	0.78
	ANN	0.83	0.84	0.80	0.82
	SVR	0.83	0.86	0.80	0.83
	RF	0.84	0.87	0.81	0.84
	XGBoost	0.86	0.88	0.78	0.84
	CatBoost	0.86	0.88	0.78	0.84
	LightGBM	0.86	0.86	0.86	0.86
	ERT	0.88	0.89	0.81	0.86
	Voting	0.88	0.89	0.85	0.87
RMSE	MDN	0.79	2.10	1.41	1.43
	ANN	0.71	1.68	1.32	1.24
	SVR	0.70	1.80	1.31	1.27
	RF	0.68	1.64	1.29	1.20
	XGBoost	0.65	1.56	1.38	1.20
	CatBoost	0.64	1.65	1.09	1.13
	LightGBM	0.63	1.56	1.39	1.19
	ERT	0.60	1.51	1.29	1.13
	Voting	0.60	1.51	1.16	1.09
MAPE	MDN	21.37%	14.17%	11.80%	15.78%
	ANN	21.23%	11.80%	10.92%	14.65%
	SVR	17.35%	10.87%	15.61%	14.61%
	RF	20.36%	10.26%	11.11%	13.91%
	XGBoost	17.86%	9.69%	10.71%	12.75%
	CatBoost	18.52%	9.69%	10.13%	12.78%
	LightGBM	18.48%	9.46%	10.28%	12.74%
	ERT	16.83%	8.71%	9.15%	11.56%

(*continued on next page*)

Table B2 (*continued*)

Performance metrics	Model	Output			Average
		MQ	MS	FV	
	Voting	16.62%	9.37%	9.89%	11.96%
MAE	MDN	0.53	1.39	0.53	0.82
	ANN	0.48	1.06	0.50	0.68
	SVR	0.47	1.16	0.64	0.76
	RF	0.46	1.04	0.50	0.67
	XGBoost	0.43	1.01	0.49	0.64
	CatBoost	0.44	1.03	0.46	0.64
	LightGBM	0.43	0.98	0.47	0.63
	ERT	0.40	0.92	0.43	0.58
	Voting	0.40	0.95	0.45	0.60

Appendix C. SHAP analysis demonstration

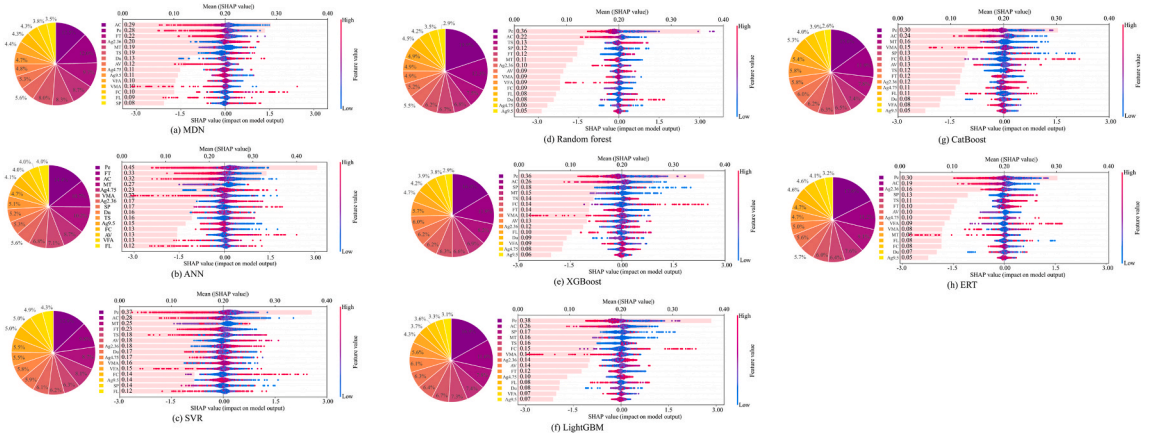

Fig. C1. Summary plot of SHAP-based interpretation of the outputs from the rest eight machine learning models: (a) MDN; (b) ANN; (c) SVR; (d) Random forest; (e) XGBoost; (f) LightGBM; (g) CatBoost; (h) ERT.

Appendix D. Inventory data used for life cycle assessment

Table. D1
Material cost, carbon footprint, and energy consumption of FRAC ingredients

Ingredient		Cost (USD/kg)	Carbon footprint (kg/kg)	Energy consumption (MJ/kg)
Fiber	Glass fiber	0.5-0.75 Khaled et al. (2024) (Khaled et al., 2024); Ali et al. (2020) (Ali et al., 2020)	2.04 Joshi et al. (2004) (Joshi et al., 2004)	48.33 Joshi et al. (2004) (Joshi et al., 2004)
	Mineral fiber	1.62-4.88 Liang et al. (2022) (Liang et al., 2022); Wang (2017) (Wang, 2017)	0.06 Ghimire (2023) (Ghimire, 2023)	0.96 Ghimire (2023) (Ghimire, 2023)
	Plastic fiber	1.11-11 Kumar et al. (2009) (Kumar et al., 2009); Wang (2008) (Wang, 2008); Kar et al. (2019) (Kar et al., 2019); Yin (2020) (Yin, 2020); Mahjoubi et al. (2021) (Mahjoubi et al., 2021)	1.96-4.08 Mahjoubi et al. (2021) (Mahjoubi et al., 2021); Choi et al. (2022) (Choi et al., 2022)	73-116 Shoji et al. (2022) (Shoji et al., 2022)
	Steel fiber	4-8 Mahjoubi et al. (2021) (Mahjoubi et al., 2021); Alsalman et al. (2020) (Alsalman et al., 2020)	1.5-3.43 Mahjoubi et al. (2021) (Mahjoubi et al., 2021); Chiaia et al. (2014) (Chiaia et al., 2014)	20.56-36 Chiaia et al. (2014) (Chiaia et al., 2014); Kathirvel and Sreekumaran (2021) (Kathirvel and Sreekumaran, 2021)
	Carbon fiber	14.1-35 Shanbara (2021) (Aljubory et al., 2021); Cheng (2010) (Cheng, 2010); Kawajiri and Sakamoto (2022) (Kawajiri and Sakamoto, 2022)	19.29-24.83 Kawajiri and Sakamoto (2022) (Kawajiri and Sakamoto, 2022)	136.8-478 Kawajiri and Sakamoto (2022) (Kawajiri and Sakamoto, 2022); Suzuki and Takahashi (2005) (Suzuki and Takahashi, 2005)
	Bio-fiber	0.21-0.98 Chen et al. (2019) (Chen et al., 2019); Ramalingam et al. (2017) (Ramalingam et al., 2017); Guan (2010) (Guan, 2010); Qin (2002) (Qin, 2002)	0.87 Bjurström et al. (2025) (Bjurström et al., 2025)	25 Bajwa et al. (2019) (Bajwa et al., 2019)
Asphalt		0.2-1.33	0.29	4.17

(*continued on next page*)

Table. D1 (*continued*)

Ingredient	Cost (USD/kg)	Carbon footprint (kg/kg)	Energy consumption (MJ/kg)
	Khaled et al. (2024) (Khaled et al., 2024); Liang et al. (2022) (Liang et al., 2022); Wang (2017) (Wang, 2017); Kumar et al. (2019) (Kumar et al., 2009); Wang (2008) (Wang, 2008); Yin (2020) (Yin, 2020)	Yang (2014) (Yang, 2014)	Yang (2014) (Yang, 2014)
Coarse aggregate	0.04-0.045 Adamu et al. (2018) (Adamu et al., 2018); Cabrera-Luna et al. (2020) (Cabrera-Luna et al., 2020)	0.0038-0.015 Song et al. (2022) (Song et al., 2022); Golafshani et al. (2021) (Golafshani et al., 2021); Thilakarathna et al. (2020) (Thilakarathna et al., 2020); de Souza et al. (2021) (de Souza et al., 2021); Bennett et al. (2022) (Bennett et al., 2022)	0.022-0.113 Chiaia et al. (2014) (Chiaia et al., 2014); Müller et al. (2014) (Müller et al., 2014)
Fine aggregate	0.014-0.04 Adamu et al. (2018) (Adamu et al., 2018); Cabrera-Luna et al. (2020) (Cabrera-Luna et al., 2020); Kumar et al. (2020) (Kumar et al., 2020)	0.0025-0.025 Mahjoubi et al. (2021) (Mahjoubi et al., 2021); Song et al. (2022) (Song et al., 2022); Golafshani et al. (2021) (Golafshani et al., 2021); Thilakarathna et al. (2020) (Thilakarathna et al., 2020); de Souza et al. (2021) (de Souza et al., 2021); Bennett et al. (2022) (Bennett et al., 2022); Naseri et al. (2020) (Naseri et al., 2020); Tavares et al. (2022) (Tavares and Grasley, 2022); Hammond et al. (2008) (Hammond et al., 2008)	0.022-0.23 Kathirvel and Sreekumaran (2021) (Kathirvel and Sreekumaran, 2021); Müller et al. (2014) (Müller et al., 2014); Zhang et al. (2020) (Zhang et al., 2020)
Filler	0.008-0.16 Chiaia et al. (2014) (Chiaia et al., 2014); Müller et al. (2014) (Müller et al., 2014); Hammond et al. (2008) (Hammond et al., 2008); Ghavami et al. (2021) (Ghavami et al., 2021); Wille et al. (2015) (Wille and Boisvert-Cotulio, 2015)	0.008-1.15 Mahjoubi et al. (2021) (Mahjoubi et al., 2021); Chiaia et al. (2014) (Chiaia et al., 2014); Song et al. (2022) (Song et al., 2022); Golafshani et al. (2021) (Golafshani et al., 2021); Thilakarathna et al. (2020) (Thilakarathna et al., 2020); de Souza et al. (2021) (de Souza et al., 2021); Naseri et al. (2020) (Naseri et al., 2020); Tavares et al. (2022) (Tavares and Grasley, 2022); Hammond et al. (2008) (Hammond et al., 2008); Ghavami et al. (2021) (Ghavami et al., 2021); Lavercombe et al. (2021) (Lavercombe et al., 2021); Park et al. (2021) (Park et al., 2021); Batuecas et al. (2021) (Batuecas et al., 2021); Wałach et al. (2019) (Wałach et al., 2019); Zheng et al. (2021) (Zheng et al., 2021); Hilton et al. (2019) (Hilton et al., 2019); Kurad et al. (2017) (Kurad et al., 2017)	0.35-5.8 Shoji et al. (2022) (Shoji et al., 2022); Alsalman et al. (2020) (Alsalman et al., 2020); Chiaia et al. (2014) (Chiaia et al., 2014); Müller et al. (2014) (Müller et al., 2014); Adamu et al. (2018) (Adamu et al., 2018); Cabrera-Luna et al. (2020) (Cabrera-Luna et al., 2020); Ghavami et al. (2021) (Ghavami et al., 2021); Ellis et al. (2017) (Ellis and McDowell, 2017)

Appendix E. Supplementary data

Supplementary data to this article can be found online at https://doi.org/10.1016/j.jclepro.2026.147759

Data availability

Data will be made available on request.

References

Adamu, M., Mohammed, B.S., Liew, M.S., 2018. Mechanical properties and performance of high volume fly ash roller compacted concrete containing crumb rubber and nano silica. Constr. Build. Mater. 171, 521–538. https://doi.org/10.1016/j.conbuildmat.2018.03.138.

Al-Atroush, M.E., 2022. Structural behavior of the geothermo-electrical asphalt pavement: a critical review concerning climate change. Heliyon 8 (12), e12107. https://doi.org/10.1016/j.heliyon.2022.e12107.

Ali, B., Qureshi, L.A., Khan, S.U., 2020. Flexural behavior of glass fiber-reinforced recycled aggregate concrete and its impact on the cost and carbon footprint of concrete pavement. Constr. Build. Mater. 262, 120820. https://doi.org/10.1016/j.conbuildmat.2020.120820.

Aljubory, A., Teama, Z.T., Salman, H.T., Abd Alkareem, H.M., 2021. Effects of cellulose fibers on the properties of asphalt mixtures. Mater. Today Proc. 42, 2941–2947. https://doi.org/10.1016/j.matpr.2020.12.772.

AlKheder, S., AlKandari, D., AlYatama, S., 2022. Sustainable assessment criteria for airport runway material selection: a fuzzy analytical hierarchy approach. Eng. Constr. Archit. Manag. 29 (8), 3091–3113. https://doi.org/10.1108/ECAM-01-2021-0052.

Alsalman, A., Dang, C.N., Martí-Vargas, J.R., Hale, W.M., 2020. Mixture-proportioning of economical UHPC mixtures. J. Build. Eng. 27, 100970. https://doi.org/10.1016/j.jobe.2019.100970.

Antkiewicz, M., Myszkowski, P.B., 2024. Balancing Pareto Front exploration of Non-dominated Tournament Genetic Algorithm (B-NTGA) in solving multi-objective NP-hard problems with constraints. Inf. Sci. 667, 120400. https://doi.org/10.1016/j.ins.2024.120400.

Arabzadeh, A., Ceylan, H., Kim, S., Gopalakrishnan, K., Sassani, A., 2016. Superhydrophobic coatings on asphalt concrete surfaces: toward smart solutions for winter pavement maintenance. Transp. Res. Rec. 2551 (1), 10–17. https://doi.org/10.3141/2551-02.

Asphalt Concrete Market Outlook (2024 to 2034). https://www.factmr.com/report/1370/asphalt-concrete-market, 2024.

Bajwa, D.S., Pourhashem, G., Ullah, A.H., Bajwa, S.G., 2019. A concise review of current lignin production, applications, products and their environmental impact. Ind. Crop. Prod. 139, 111526. https://doi.org/10.1016/j.indcrop.2019.111526.

Bartlett, P., Freund, Y., Lee, W.S., Schapire, R.E., 1998. Boosting the margin: a new explanation for the effectiveness of voting methods. Ann. Stat. 26 (5), 1651–1686. https://doi.org/10.1214/aos/1024691352.

Batuecas, E., Ramón-Álvarez, I., Sánchez-Delgado, S., Torres-Carrasco, M., 2021. Carbon footprint and water use of alkali-activated and hybrid cement mortars. J. Clean. Prod. 319, 128653. https://doi.org/10.1016/j.jclepro.2021.128653.

Benesty, J., Chen, J., Huang, Y., Cohen, I., 2009. Pearson correlation coefficient. Noise Reduction in Speech Processing. Springer Berlin Heidelberg, Berlin, Heidelberg, pp. 1–4. https://doi.org/10.1007/978-3-642-00296-0_5.

Bennett, B., Visintin, P., Xie, T., 2022. Global warming potential of recycled aggregate concrete with supplementary cementitious materials. J. Build. Eng. 52, 104394. https://doi.org/10.1016/j.jobe.2022.104394.

Bergstra, J., Bengio, Y., 2012. Random search for hyper-parameter optimization. J. Mach. Learn. Res. 13 (1), 281–305. https://dl.acm.org/doi/10.5555/2188385.2188395.

Bieliatynskyi, A., Yang, S., Pershakov, V., Shao, M., Ta, M., 2022. Features of the hot recycling method used to repair asphalt concrete pavements. Materials Science-Poland 40 (2), 181–195. https://doi.org/10.2478/msp-2022-0021.

Bishop, C.M., 1994. Mixture density networks. https://publications.aston.ac.uk/id/eprint/373/1/NCRG_94_004.pdf.

Bjurström, A., Hedenqvist, M.S., Prade, T., Mensah, R.A., Das, O., Åhrlin, A., Matsson, A., Helgesson, D., Carrick, C., Roulin, T., Gorur, Y., Jerpdal, L., Bruder, S., Wei, X.F., 2025. Synergistic enhancement of fire performance and carbon footprint reduction in polymer biocomposites through combined use of lignin and biochar. Ind. Crop. Prod. 233, 121402. https://doi.org/10.1016/j.indcrop.2025.121402.

Cabrera-Luna, K., Maldonado-Bandala, E.E., Nieves-Mendoza, D., Castro-Borges, P., García, J.E., 2020. Novel low emissions supersulfated cements of pumice in concrete; mechanical and electrochemical characterization. J. Clean. Prod. 272, 122520. https://doi.org/10.1016/j.jclepro.2020.122520.

Calvert, R.L., 1985. Robustness of the multidimensional voting model: candidate motivations, uncertainty, and convergence. Am. J. Polit. Sci. 69–95. https://doi.org/10.2307/2111212.

Chen, T., Guestrin, C., 2016. XGBoost: a scalable tree boosting system. Proceedings of the 22nd ACM SIGKDD International Conference on Knowledge Discovery and Data Mining 785–794. https://doi.org/10.1145/2939672.2939785.

Chen, Z., Chen, Z., Yi, J., Feng, D., 2019. Preparation method of corn stalk fiber material and its performance investigation in asphalt concrete. Sustainability 11 (15), 4050. https://doi.org/10.3390/su11154050.

Cheng, J., 2010. Research on Conductive Asphalt Concrete with PAN-based Carbon Fiber. Master's Thesis. Changsha University of Science and Technology. https://kns.cnki.net/kcms2/article/abstract?v=5q1osi_AJORyQfRv7nOs7295RCRjdqcsPqw6GqtS_z4IL1TTlzyiZGQiAwkpGwTGWJq50ClNkB4rRk3AuSpoEtR9MGKXxhsOzeiPeuFsumvVox5qYvhOSh0aHHAan1qo-JGEB6w5gYikk6l7Ifw9rB_CMw8F0hk8fSnDNuXZmis=&uniplatform=NZKPT.

Chiaia, B., Fantilli, A.P., Guerini, A., Volpatti, G., Zampini, D., 2014. Eco-mechanical index for structural concrete. Constr. Build. Mater. 67, 386–392. https://doi.org/10.1016/j.conbuildmat.2013.12.090.

Choi, J.I., Park, S.E., Kim, Y., Yang, K., Kim, Y.Y., Lee, B.Y., 2022. Highly ductile behavior and sustainability of engineered cementitious composites reinforced by PE based selvage fibers. Cement Concr. Compos. 134, 104729. https://doi.org/10.1016/j.cemconcomp.2022.104729.

Cortes, C., Vapnik, V., 1995. Support-vector networks. Mach. Learn. 20, 273–297. https://doi.org/10.1007/BF00994018.

de Souza, A.M., de Lima, G.E.S., Nalon, G.H., Lopes, M.M.S., de Oliveira Júnior, A.L., Lopes, G.J.R., Olivier, M.JeA., Pedroti, L.G., Ribeiro, J.C.L., de Carvalho, J.M.F., 2021. Application of the desirability function for the development of new composite eco-efficiency indicators for concrete. J. Build. Eng. 40, 102374. https://doi.org/10.1016/j.jobe.2021.102374.

Deb, K., Agrawal, S., Pratap, A., Meyarivan, T., 2000. A fast elitist non-dominated sorting genetic algorithm for multi-objective optimization: NSGA-II. In: International Conference on Parallel Problem Solving from Nature. Springer Berlin Heidelberg, Berlin, Heidelberg, pp. 849–858. https://doi.org/10.1007/3-540-45356-3_83.

Deb, K., Pratap, A., Agarwal, S., Meyarivan, T.A.M.T., 2002. A fast and elitist multiobjective genetic algorithm: NSGA-II. IEEE Trans. Evol. Comput. 6 (2), 182–197. https://doi.org/10.1109/4235.996017.

Dias, J.F., Picado-Santos, L.G., Capitão, S.D., 2014. Mechanical performance of dry process fine crumb rubber asphalt mixtures placed on the Portuguese road network. Constr. Build. Mater. 73, 247–254. https://doi.org/10.1016/j.conbuildmat.2014.09.110.

Dietterich, T.G., 2000. Ensemble methods in machine learning. International Workshop on Multiple Classifier Systems. Springer Berlin Heidelberg, Berlin, Heidelberg, pp. 1–15. https://doi.org/10.1007/3-540-45014-9_1.

Ejaz, U., Khan, S.M., Jehangir, S., Ahmad, Z., Abdullah, A., Iqbal, M., Khalid, N., Nazir, A., Svenning, J.C., 2024. Monitoring the industrial waste polluted stream-integrated analytics and machine learning for water quality index assessment. J. Clean. Prod. 450, 141877. https://doi.org/10.1016/j.jclepro.2024.141877.

Ellis, B.D., McDowell, D.L., 2017. Application-specific computational materials design via multiscale modeling and the inductive design exploration method (IDEM). Integrating Materials and Manufacturing Innovation 6, 9–35. https://doi.org/10.1007/s40192-017-0086-3.

García, A., Norambuena-Contreras, J., Bueno, M., Partl, M.N., 2014. Influence of steel wool fibers on the mechanical, termal, and healing properties of dense asphalt concrete. J. Test. Eval. 42 (5), 1107–1118. https://doi.org/10.1520/JTE20130197.

Ge, D., Jin, D., Liu, C., Gao, J., Yu, M., Malburg, L., You, Z., 2022. Laboratory performance and field case study of asphalt mixture with sasobit treated aramid fiber as modifier. Transp. Res. Rec. 2676 (2), 811–824. https://doi.org/10.1177/03611981211047833.

Geurts, P., Ernst, D., Wehenkel, L., 2006. Extremely randomized trees. Mach. Learn. 63, 3–42. https://doi.org/10.1007/s10994-006-6226-1.

Ghavami, S., Naseri, H., Jahanbakhsh, H., Nejad, F.M., 2021. The impacts of nano-SiO_2 and silica fume on cement kiln dust treated soil as a sustainable cement-free stabilizer. Constr. Build. Mater. 285, 122918. https://doi.org/10.1016/j.conbuildmat.2021.122918.

Ghimire, A., 2023. Life cycle assessment of glass fiber or basalt fiber composite baseball Bats: a comparative environmental analysis. Bachelor's Thesis. Arcada University of Applied Sciences. https://urn.fi/URN:NBN:fi:amk-2023122138961.

Golafshani, E.M., Arashpour, M., Kashani, A., 2021. Green mix design of rubbercrete using machine learning-based ensemble model and constrained multi-objective optimization. J. Clean. Prod. 327, 129518. https://doi.org/10.1016/j.jclepro.2021.129518.

Goodfellow, I., Bengio, Y., Courville, A., 2016. Deep Learning. MIT Press. https://dl.acm.org/doi/book/10.5555/3086952.

Guan, P., 2010. Study on the pavement performance of sisal fibers asphalt concrete. *Master's Thesis, Wuhan Institute of Technology*. URL: https://kns.cnki.net/kcms2/article/abstract?v=5q1osi_AJOQcKESrjaiEbUDFnZx5DxxF05HWDipUUp3bFZYX2cp5cdJkQMgSX_RrntA5dNrXK4MjGygHV5An3qYpnHgH3kPVvi2ALp5zUrcVe84d6y_32tB1gD7SSXKt7oxOKWWH5BlJGKoMbiGmy9O3nDa3n3wY7w5KWiMotjw=&uniplatform=NZKPT.

Guo, P., Meng, W., Bao, Y., 2024. Knowledge-guided data-driven design of ultra-high-performance geopolymer (UHPG). Cement Concr. Compos. 153, 105723. https://doi.org/10.1016/j.cemconcomp.2024.105723.

Hammond, G., Jones, C., Lowrie, F., Tse, P., 2008. The Inventory of Carbon and Energy (ICE). Sustainable Energy Research Team, Department of Mechanical Engineering, University of Bath. https://kps.fsv.cvut.cz/upload/files/icev2.0summarytables.pdf.

Hejazi, S.M., Abtahi, S.M., Sheikhzadeh, M., Semnani, D., 2008. Introducing two simple models for predicting fiber-reinforced asphalt concrete behavior during longitudinal loads. J. Appl. Polym. Sci. 109 (5), 2872–2881. https://doi.org/10.1002/app.28349.

Hilton, B., Bawden, K., Winnebeck, K., Chandrasiri, C., Ariyachandra, E., Peethamparan, S., 2019. The functional and environmental performance of mixed cathode ray tubes and recycled glass as partial replacement for cement in concrete. Resour. Conserv. Recycl. 151, 104451. https://doi.org/10.1016/j.resconrec.2019.104451.

Huang, Y., Bird, R.N., Heidrich, O., 2007. A review of the use of recycled solid waste materials in asphalt pavements. Resour. Conserv. Recycl. 52 (1), 58–73. https://doi.org/10.1016/j.resconrec.2007.02.002.

Jain, A., Nandakumar, K., Ross, A., 2005. Score normalization in multimodal biometric systems. Pattern Recogn. 38 (12), 2270–2285. https://doi.org/10.1016/j.patcog.2005.01.012.

James, W., Thompson, M.K., 2021. Contaminants from four new pervious and impervious pavements in a parking-lot. Advances in Modeling the Management of Stormwater Impacts. CRC Press, pp. 207–222. https://doi.org/10.1201/9781003208945.

Jin, D., Ge, D., Zhou, X., You, Z., 2022a. Asphalt mixture with scrap tire rubber and nylon fiber from waste tires: laboratory performance and preliminary ME design analysis. Buildings 12 (2), 160. https://doi.org/10.3390/buildings12020160.

Jin, D., Boateng, K.A., Chen, S., Xin, K., You, Z., 2022b. Comparison of rubber asphalt with polymer asphalt under long-term aging conditions in Michigan. Sustainability 14 (17), 10987. https://doi.org/10.3390/su141710987.

Joshi, S.V., Drzal, L.T., Mohanty, A.K., Arora, S., 2004. Are natural fiber composites environmentally superior to glass fiber reinforced composites? Compos. Appl. Sci. Manuf. 35 (3), 371–376. https://doi.org/10.1016/j.compositesa.2003.09.016.

Kar, S.S., Nagabhushana, M.N., Jain, P.K., 2019. Performance of hot bituminous mixes admixed with blended synthetic fibers. International Journal of Pavement Research and Technology 12 (4), 370–379. https://doi.org/10.1007/s42947-019-0044-x.

Karanam, G.D., Underwood, B.S., 2024. Mechanical characterization and performance prediction of fiber-modified asphalt mixes. International Journal of Pavement Research and Technology 1–19. https://doi.org/10.1007/s42947-024-00445-9.

Kathirvel, P., Sreekumaran, S., 2021. Sustainable development of ultra high performance concrete using geopolymer technology. J. Build. Eng. 39, 102267. https://doi.org/10.1016/j.jobe.2021.102267.

Kaveh, A., 2024. Applications of Artificial Neural Networks and Machine Learning in Civil Engineering. Springer. https://doi.org/10.1007/978-3-031-66051-1.

Kawajiri, K., Sakamoto, K., 2022. Environmental impact of carbon fibers fabricated by an innovative manufacturing process on life cycle greenhouse gas emissions. Sustain. Mater. Technol. 31, e00365. https://doi.org/10.1016/j.susmat.2021.e00365.

Ke, G., Meng, Q., Finley, T., Wang, T., Chen, W., Ma, W., Ye, Q., Liu, T.Y., 2017. LightGBM: a highly efficient gradient boosting decision tree. Proceedings of the 31st International Conference on Neural Information Processing Systems, pp. 3149–3157. In: https://proceedings.neurips.cc/paper/2017/file/6449f44a102fde848669bdd9eb6b76fa-Paper.pdf.

Khaled, T.T., Kareem, A.I., Mohamad, S.A., Al-Hamd, R.K.S., Minto, A., 2024. The performance of modified asphalt mixtures with different lengths of glass fiber. International Journal of Pavement Research and Technology 1–17. https://doi.org/10.1007/s42947-024-00443-x.

Khan, M., Lao, J., Dai, J.G., 2022. Comparative study of advanced computational techniques for estimating the compressive strength of UHPC. Journal of Asian Concrete Federation 8 (1), 51–68. https://doi.org/10.18702/acf.2022.6.8.1.51.

Khan, A.R., Ali, A., Pandya, H., Alfalah, A., Mehta, Y., Elshaer, M., Decarlo, C., 2023a. Assessment of the impact of binder grade on the laboratory performance of fiber reinforced asphalt mixtures. Constr. Build. Mater. 401, 132735. https://doi.org/10.1016/j.conbuildmat.2023.132735.

Khan, A.R., Fareed, A., Ali, A., Pandya, H., Ali, A., Mehta, Y., 2023b. Seasonal performance prediction comparison of unreinforced and fiber-reinforced Asphalt mixtures for airfield pavements. In: Airfield and Highway Pavements 2023, pp. 374–384. https://doi.org/10.1061/9780784484890.034.

Khan, A.R., Ali, A., Mehta, Y., Lein, W., 2024. Laboratory performance characterization of polyolefin/aramid fibers and synthetic aramid fibers reinforced asphalt mixtures. Constr. Build. Mater. 419, 135576. https://doi.org/10.1016/j.conbuildmat.2024.135576.

Kumar, P., Mehndiratta, H.C., Immadi, S., 2009. Investigation of fiber-modified bituminous mixes. Transp. Res. Rec. 2126 (1), 91–99. https://doi.org/10.3141/2126-11.

Kumar, C., Yaragal, S.C., Das, B.B., 2020. Ferrochrome ash–its usage potential in alkali activated slag mortars. J. Clean. Prod. 257, 120577. https://doi.org/10.1016/j.jclepro.2020.120577.

Kurad, R., Silvestre, J.D., de Brito, J., Ahmed, H., 2017. Effect of incorporation of high volume of recycled concrete aggregates and fly ash on the strength and global warming potential of concrete. J. Clean. Prod. 166, 485–502. https://doi.org/10.1016/j.jclepro.2017.07.236.

Lavercombe, A., Huang, X., Kaewunruen, S., 2021. Machine learning application to eco-friendly concrete design for decarbonisation. Sustainability 13 (24), 13663. https://doi.org/10.3390/su132413663.

Li, L., Khan, M., Jiang, X., Shakor, P., Zhang, Y., 2023. Sustainable fiber reinforced cementitious composites for construction and building materials. Front. Mater. 10, 1237960. https://doi.org/10.3389/fmats.2023.1237960.

Liang, R., Yu, W., Luo, Z., 2022. Laboratory investigation on pavement performance of basalt fiber-reinforced asphalt mixture under the coupling effect of freeze-thaw cycles and aging. Front. Mater. 9, 930056. https://doi.org/10.3389/fmats.2022.930056.

Lipton, Z.C., 2018. The mythos of model interpretability: in machine learning, the concept of interpretability is both important and slippery. ACM Queue 16 (3), 31–57. https://doi.org/10.1145/3233231.

Liu, Q.T., Wu, S.P., 2014. Effects of steel wool distribution on properties of porous asphalt concrete. Key Eng. Mater. 599, 150–154. https://doi.org/10.4028/www.scientific.net/KEM.599.150.

Lundberg, S.M., Lee, S.I., 2017. A unified approach to interpreting model predictions. Proceedings of the 31st International Conference on Neural Information Processing Systems, pp. 4768–4777. https://dl.acm.org/doi/10.5555/3295222.3295230.

Ma, J., Hesp, S.A., 2022. Effect of recycled polyethylene terephthalate (PET) fiber on the fracture resistance of asphalt mixtures. Constr. Build. Mater. 342, 127944. https://doi.org/10.1016/j.conbuildmat.2022.127944.

Ma, Y., Zhou, H., Jiang, X., Polaczyk, P., Xiao, R., Zhang, M., Huang, B., 2021. The utilization of waste plastics in asphalt pavements: a review. Clean. Mater. 2, 100031. https://doi.org/10.1016/j.clema.2021.100031.

Ma, J., Nawarathna, H.M., Hesp, S.A., 2022. On the sustainable use of recycled plastics in flexible asphalt pavements. J. Clean. Prod. 359, 132081. https://doi.org/10.1016/j.jclepro.2022.132081.

Ma, Y., Polaczyk, P., Zhang, M., Xiao, R., Jiang, X., Huang, B., 2023. Comparative study of pavement rehabilitation using hot in-place recycling and hot-mix asphalt: performance evaluation, pavement life prediction, and life cycle cost analysis. Transp. Res. Rec. 2677 (1), 420–431. https://doi.org/10.1177/03611981221099907.

Ma, R., Li, Y., Cheng, P., Chen, X., Cheng, A., 2024a. Low-temperature cracking and improvement methods for asphalt pavement in cold regions: a review. Buildings 14 (12), 3802. https://doi.org/10.3390/buildings14123802.

Ma, J., Yuan, H., Nawarathna, H.M., Hesp, S.A., 2024b. Sustainable application of recycled plastics in asphalt pavement: case study of a trial in Newtonville, Ontario, Canada. Can. J. Civ. Eng. 52 (5), 597–612. https://doi.org/10.1139/cjce-2024-0438.

Mahjoubi, S., Barhemat, R., Guo, P., Meng, W., Bao, Y., 2021. Prediction and multi-objective optimization of mechanical, economical, and environmental properties for strain-hardening cementitious composites (SHCC) based on automated machine learning and metaheuristic algorithms. J. Clean. Prod. 329, 129665. https://doi.org/10.1016/j.jclepro.2021.129665.

Mateos, A., Harvey, J., 2019. Laboratory Evaluation of the Mechanical Properties of Asphalt Concrete Reinforced with Aramid Synthetic Fibers. Research Report: UCPRC-RR-2019-01. Institute of Transportation Studies, UC Berkeley. https://escholarship.org/uc/item/40j1p8k7.

Müller, H.S., Haist, M., Vogel, M., 2014. Assessment of the sustainability potential of concrete and concrete structures considering their environmental impact, performance and lifetime. Constr. Build. Mater. 67, 321–337. https://doi.org/10.1016/j.conbuildmat.2014.01.039.

Naseri, H., Jahanbakhsh, H., Hosseini, P., Nejad, F.M., 2020. Designing sustainable concrete mixture by developing a new machine learning technique. J. Clean. Prod. 258, 120578. https://doi.org/10.1016/j.jclepro.2020.120578.

Ning, Z., Sun, Z., Liu, Y., Dong, J., Meng, X., Wang, Q., Wei, Y., 2024. Evaluating the impervious performance of hydraulic asphalt concrete in embankment dams: a study of crack evolution at different temperatures. Constr. Build. Mater. 440, 137247. https://doi.org/10.1016/j.conbuildmat.2024.137247.

Park, K.B., Lin, R.S., Han, Y., Wang, X.Y., 2021. Model-based methods to produce greener metakaolin composite concrete. Appl. Sci. 11 (22), 10704. https://doi.org/10.3390/app112210704.

Pasandín, A.R., Pérez, I., 2015. Overview of bituminous mixtures made with recycled concrete aggregates. Constr. Build. Mater. 74, 151–161. https://doi.org/10.1016/j.conbuildmat.2014.10.035.

Phung, B.N., Le, T.H., Nguyen, M.K., Nguyen, T.A., Ly, H.B., 2023a. Practical numerical tool for marshall stability prediction based on machine learning: an application for asphalt concrete containing basalt fiber. Journal of Science and Transport Technology 26–43. https://doi.org/10.58845/jstt.utt.2023.en.3.3.26-43.

Phung, B.N., Le, T.H., Nguyen, T.A., Hoang, H.G.T., Ly, H.B., 2023b. Novel approaches to predict the Marshall parameters of basalt fiber asphalt concrete. Constr. Build. Mater. 400, 132847. https://doi.org/10.1016/j.conbuildmat.2023.132847.

Prokhorenkova, L., Gusev, G., Vorobev, A., Dorogush, A.V., Gulin, A., 2018. CatBoost: unbiased boosting with categorical features. Adv. Neural Inf. Process. Syst. 31. In: https://proceedings.neurips.cc/paper/2018/hash/14491b756b3a51daac41c24863285549-Abstract.html.

Qin, Y., 2002. Research on the Road Performance and Application of High-Performance Asphalt Mixtures. Master's Thesis. Dalian University of Technology. https://kns.cnki.net/kcms2/article/abstract?v=5q1osi_AJOS0Sw5dXXhyWBiRKa_EV86O76HtPhIkg7-nYRT-6itSLL7_QBhSh6jJ7q1tVHHD61P_r5dtxAj3Mgm_k0HlC62p28hOAS3GwU_27m2iGATZvCu1lUD3TBTWEM1WwkRo3-_2jvjYQZBfRqCN-Fhxe5Uz7AhvaVGkuQs=&uniplatform=NZKPT.

Ramalingam, S., Murugasan, R., Nagabhushana, M.N., 2017. Laboratory performance evaluation of environmentally sustainable sisal fibre reinforced bituminous mixes. Constr. Build. Mater. 148, 22–29. https://doi.org/10.1016/j.conbuildmat.2017.05.006.

Rivera-Pérez, J., Talebpour, A., Al-Qadi, I.L., 2023. Prediction of asphalt concrete flexibility index and rut depth utilising deep learning and Monte Carlo Dropout simulation. Int. J. Pavement Eng. 24 (1), 2253964. https://doi.org/10.1080/10298436.2023.2253964.

Shimizu, S., Hoyer, P.O., Hyvärinen, A., Kerminen, A., Jordan, M., 2006. A linear Non-Gaussian acyclic model for causal discovery. J. Mach. Learn. Res. 7 (10), 2003–2030. https://dl.acm.org/doi/abs/10.5555/1248547.1248619.

Shoji, D., He, Z., Zhang, D., Li, V.C., 2022. The greening of engineered cementitious composites (ECC): a review. Constr. Build. Mater. 327, 126701. https://doi.org/10.1016/j.conbuildmat.2022.126701.

Singh, D., Singh, B., 2020. Investigating the impact of data normalization on classification performance. Appl. Soft Comput. 97, 105524. https://doi.org/10.1016/j.asoc.2019.105524.

Song, Y., Ouyang, B., Chen, J., Wang, X., Wang, K., Zhang, S., Chen, Y., Sant, G., Bauchy, M., 2022. Decarbonizing concrete with artificial intelligence. Computational Modelling of Concrete and Concrete Structures. CRC Press, pp. 168–176. https://doi.org/10.1201/9781003316404.

Sun, Y., Ding, S., Zhang, Z., Jia, W., 2021. An improved grid search algorithm to optimize SVR for prediction. Soft Comput. 25, 5633–5644. https://doi.org/10.1007/s00500-020-05560-w.

Suzuki, T., Takahashi, J., 2005. Prediction of energy intensity of carbon fiber reinforced plastics for mass-produced passenger cars. Proceedings of 9th Japan International SAMPE Symposium, pp. 14–19. https://www.researchgate.net/publication/264838761.

Takaikaew, T., Tepsriha, P., Horpibulsuk, S., Hoy, M., Kaloush, K.E., Arulrajah, A., 2018. Performance of fiber-reinforced asphalt concretes with various asphalt binders in Thailand. J. Mater. Civ. Eng. 30 (8), 04018193. https://doi.org/10.1061/(ASCE)MT.1943-5533.0002433.

Takaikaew, T., Hoy, M., Horpibulsuk, S., Arulrajah, A., Mohammadinia, A., Horpibulsuk, J., 2021. Performance improvement of asphalt concretes using fiber reinforcement. Heliyon 7 (5), e07015. https://doi.org/10.1016/j.heliyon.2021.e07015.

Tan, X., Mahjoubi, S., Zhang, Q., Dong, D., Bao, Y., 2022. A framework for improving bridge resilience and sustainability through optimizing high-performance fiber-reinforced cementitious composites. Journal of Infrastructure Preservation and Resilience 3 (1), 18. https://doi.org/10.1186/s43065-022-00067-0.

Tavares, C., Grasley, Z., 2022. Machine learning-based mix design tools to minimize carbon footprint and cost of UHPC. Part 2: cost and eco-efficiency density diagrams. Clean. Mater. 4, 100094. https://doi.org/10.1016/j.clema.2022.100094.

Taylor, K.E., Stouffer, R.J., Meehl, G.A., 2012. An overview of CMIP5 and the experiment design. Bull. Am. Meteorol. Soc. 93 (4), 485–498. https://doi.org/10.1175/BAMS-D-11-00094.1.

Thilakarathna, P.S.M., Seo, S., Baduge, K.K., Lee, H., Mendis, P., Foliente, G., 2020. Embodied carbon analysis and benchmarking emissions of high and ultra-high strength concrete using machine learning algorithms. J. Clean. Prod. 262, 121281. https://doi.org/10.1016/j.jclepro.2020.121281.

Upadhya, A., Thakur, M.S., Al Ansari, M.S., Malik, M.A., Alahmadi, A.A., Alwetaishi, M., Alzaed, A.N., 2022. Marshall stability prediction with glass and carbon fiber modified asphalt mix using machine learning techniques. Materials 15 (24), 8944. https://doi.org/10.3390/ma15248944.

Upadhya, A., Thakur, M.S., Sihag, P., 2024. Predicting Marshall stability of carbon fiber-reinforced asphalt concrete using machine learning techniques. International Journal of Pavement Research and Technology 17 (1), 102–122. https://doi.org/10.1007/s42947-022-00223-5.

Wałach, D., Dybeł, P., Sagan, J., Gicala, M., 2019. Environmental performance of ordinary and new generation concrete structures—a comparative analysis. Environ. Sci. Pollut. Control Ser. 26, 3980–3990. https://doi.org/10.1007/s11356-018-3804-2.

Wang, L., 2008. Research of polyester fiber reinforced asphalt mixture performance and engineering application. Master's Thesis. Hefei University of Technology. https://kns.cnki.net/kcms2/article/abstract?v=5q1osi_AJORFTZ27iE-wuKWnp4ag-pCnnjg-OvM7t86kzeVd9uHKoRGJtWHf-Vy0KJLnkFANnQ5j5Fxv0q5k3yrTXfwdMID6hdRraYa7iafht2xI4FHw8e0n2PqAV_X1dEE-O8NboHsqvfvldzRKJQjYz68IEpTIqsWKJUXUsXU=&uniplatform=NZKPT.

Wang, F., 2017. Study on the Application of Basalt Fiber Asphalt Mixture. *Master's Thesis*. Chang 'an University. https://kns.cnki.net/kcms2/article/abstract?v=5q1osi_AJOT6ymxBNinUGue5XM0JMe9LSqChkJsShdMVHbjfrEUDxvqz49YpJE18n20GGAEIdcLQ5FwYOdrxc9P7jZ7KlmOSomEWEXp5LPNPyVSG3ztqhDUkrEufII4ZVvdWhZz-r_RUh7KiSLeBo7FHFdZd73T0ChqnaPx5Xgc=&uniplatform=NZKPT.

Wang, L., Zhang, J., Song, M., Tian, B., Li, K., Liang, Y., Han, J., Wu, Z., 2017. A shell-crosslinked polymeric micelle system for pH/redox dual stimuli-triggered DOX on-demand release and enhanced antitumor activity. Colloids Surf. B Biointerfaces 152, 1–11. https://doi.org/10.1016/j.colsurfb.2016.12.032.

Wang, F., Hoff, I., Yang, F., Wu, S., Xie, J., Li, N., Zhang, L., 2021. Comparative assessments for environmental impacts from three advanced asphalt pavement construction cases. J. Clean. Prod. 297, 126659. https://doi.org/10.1016/j.jclepro.2021.126659.

Wang, J., Xiong, Y., Li, Q., Jin, D., Hu, Y., Che, T., 2023. Experimental investigation on the preparation and surface treatment of biomass fibers for stone mastic asphalt mixtures modification. Constr. Build. Mater. 408, 133667. https://doi.org/10.1016/j.conbuildmat.2023.133667.

Wille, K., Boisvert-Cotulio, C., 2015. Material efficiency in the design of ultra-high performance concrete. Constr. Build. Mater. 86, 33–43. https://doi.org/10.1016/j.conbuildmat.2015.03.087.

Wu, J., Chen, X.Y., Zhang, H., Xiong, L.D., Lei, H., Deng, S.H., 2019. Hyperparameter optimization for machine learning models based on Bayesian optimization. Journal

of Electronic Science and Technology 17 (1), 26–40. https://doi.org/10.11989/JEST.1674-862X.80904120.

Wu, M., You, Z., Jin, D., Yin, L., Xin, K., 2024. Aging effects on asphalt adhesive properties: molecular dynamics simulation of chemical composition and structural changes. Mol. Simul. 50 (13), 836–854. https://doi.org/10.1080/08927022.2024.2359568.

Yang, R., 2014. Development of a Pavement Life Cycle Assessment Tool Utilizing Regional Data and Introducing an Asphalt Binder Model. Doctoral dissertation. University of Illinois at Urbana-Champaign. https://hdl.handle.net/2142/50651.

Yao, H., Wang, Y., Ma, P., Li, X., You, Z., 2023. A literature review: asphalt pavement repair technologies and materials. Proceedings of the Institution of Civil Engineers-Engineering Sustainability 177 (5), 259–273. https://doi.org/10.1680/jensu.22.10000.

Yin, J., 2020. The feasibility of waste nylon filament used as reinforcement in asphalt mixture. International Journal of Pavement Research and Technology 13 (2), 212–221. https://doi.org/10.1007/s42947-020-0223-9.

Zaumanis, M., Mallick, R.B., Frank, R., 2016. 100% hot mix asphalt recycling: challenges and benefits. Transp. Res. Procedia 14, 3493–3502. https://doi.org/10.1016/j.trpro.2016.05.315.

Zhang, D., Jaworska, B., Zhu, H., Dahlquist, K., Li, V.C., 2020. Engineered Cementitious Composites (ECC) with limestone calcined clay cement (LC3). Cement Concr. Compos. 114, 103766. https://doi.org/10.1016/j.cemconcomp.2020.103766.

Zhang, M., Gong, H., Xiao, R., Jiang, X., Ma, Y., Huang, B., 2023. Life-cycle cost analysis of rehabilitation strategies for asphalt pavements based on probabilistic models. Road Mater. Pavement Des. 24 (1), 121–137. https://doi.org/10.1080/14680629.2021.2012235.

Zheng, C., Zhang, H., Cai, X., Chen, L., Liu, M., Lin, H., Wang, X., 2021. Characteristics of CO2 and atmospheric pollutant emissions from China's cement industry: a life-cycle perspective. J. Clean. Prod. 282, 124533. https://doi.org/10.1016/j.jclepro.2020.124533.

Zhou, C., Wang, W., Zheng, Y., 2024. Data-driven shear capacity analysis of headed stud in steel-UHPC composite structures. Eng. Struct. 321, 118946. https://doi.org/10.1016/j.engstruct.2024.118946.